NUCL SCI TECH (2024)35:217
https://doi.org/10.1007/s41365-024-01590-3

Recent progress in nuclear astrophysics research and its astrophysical implications at the China Institute of Atomic Energy

Wei-Ping Liu[1,2,3] · Bing Guo[1,3,4] · Zhu An[5] · Bao-Qun Cui[1] · Xiao Fang[6] · Chang-Bo Fu[7] · Bin-Shui Gao[8,9,10] · Jian-Jun He[11] · Yu-Chen Jiang[1] · Chong Lv[1] · Er-Tao Li[12] · Ge-Xing Li[1,3] · Yun-Ju Li[1] · Zhi-Hong Li[1,3] · Gang Lian[1,3] · Wei-Ping Lin[5] · Yi-Hui Liu[1] · Wei Nan[1] · Wei-Ke Nan[1] · Yang-Ping Shen[1,3] · Na Song[1] · Jun Su[13] · Liang-Ting Sun[14] · Xiao-Dong Tang[8,9,10] · Luo-Huan Wang[15] · Shuo Wang[16] · You-Bao Wang[1] · Di Wu[1,17] · Xiao-Feng Xi[1] · Sheng-Quan Yan[1] · Li-Yong Zhang[11]

Received: 26 June 2024 / Revised: 15 October 2024 / Accepted: 16 October 2024

Abstract Nuclear astrophysics is a rapidly developing interdisciplinary field of research that has received extensive attention from the scientific community since the mid-twentieth century. Broadly, it uses the laws of extremely small atomic nuclei to explain the evolution of the universe. Owing to the complexity of nucleosynthesis processes and our limited understanding of nuclear physics in astrophysical environments, several critical astrophysical problems remain unsolved. To achieve a better understanding of astrophysics, it is necessary to measure the cross sections of key nuclear reactions with the precision required by astrophysical models. Direct measurement of nuclear reaction cross sections is an important method of investigating how nuclear reactions influence stellar evolution. Given the challenges involved in measuring the extremely low cross

Dedicated to Professor Wenqing Shen in honour of his 80th birthday. This work was supported by the National Natural Science Foundation of China (Nos. 12435010), and the National Key R&D Program of China (No. 2022YFA1602301).

✉ Wei-Ping Liu
liuwp@sustech.edu.cn

Bing Guo
guobing@ciae.ac.cn

[1] China Institute of Atomic Energy, Beijing 102413, China

[2] Department of Physics, Southern University of Science and Technology, Shenzhen 518055, China

[3] Jinping Deep Underground Frontier Science and Dark Matter Key Laboratory of Sichuan Province, Liangshan 615000, China

[4] School of Physics, Xi'an Jiaotong University, Xi'an 710049, China

[5] Key Laboratory of Radiation Physics and Technology of the Ministry of Education, Institute of Nuclear Science and Technology, Sichuan University, Chengdu 610064, China

[6] Sino-French Institute of Nuclear Engineering and Technology, Sun Yat-sen University, Zhuhai 519082, China

[7] Key Laboratory of Nuclear Physics and Ion-beam Application (MoE), Institute of Modern Physics, Fudan University, Shanghai 200433, China

[8] Joint Department for Nuclear Physics, Institute of Modern Physics, Chinese Academy of Sciences and Lanzhou University, Lanzhou 730000, China

[9] CAS Key Laboratory of High Precision Nuclear Spectroscopy, Institute of Modern Physics, Chinese Academy of Sciences, Lanzhou 73000, China

[10] School of Nuclear Science and Technology, University of Chinese Academy of Sciences, Beijing 100049, China

[11] Key Laboratory of Beam Technology of Ministry of Education, College of Nuclear Science and Technology, Beijing Normal University, Beijing 100875, China

[12] College of Physics and Optoelectronic Engineering, Shenzhen University, Shenzhen, China

[13] Key Laboratory of Beam Technology and Material Modification of Ministry of Education, College of Nuclear Science and Technology, Beijing Normal University, Beijing 100875, China

[14] Institute of Modern Physics, Chinese Academy of Sciences, Lanzhou 730000, China

[15] School of Mathematics and Physics, Handan University, Handan 056005, China

[16] Shandong Provincial Key Laboratory of Optical Astronomy and Solar-Terrestrial Environment, Institute of Space Sciences, Shandong University, Weihai 264209, China

[17] State Key Laboratory of Nuclear Physics and Technology, School of Physics, CAPT, Peking University, Beijing 100871, China

Published online: 30 November 2024

sections of nuclear reactions in the Gamow peak and preparing radioactive targets, indirect methods, such as the transfer reaction, coulomb dissociation, and surrogate ratio methods, have been developed over the past several decades. These are powerful tools in the investigation of, for example, neutron-capture (n,γ) reactions with short-lived radioactive isotopes. However, direct measurement is still preferable, such as in the case of reactions involving light and stable nuclei. As an essential part of stellar evolution, these low-energy stable nuclear reactions have been of particular interest in recent years. To overcome the difficulties in measurements near or deeply within the Gamow window, the combination of an underground laboratory and high-exposure accelerator/detector complex is currently the optimal solution. Therefore, underground experiments have emerged as a new and promising direction of research. In addition, to better simulate the stellar environment in the laboratory, research on nuclear physics under laser-driven plasma conditions has gradually become a frontier hotspot. In recent years, the CIAE team conducted a series of distinctive nuclear astrophysics studies, relying on the Jinping Underground Nuclear Astrophysics platform and accelerators in Earth's surface laboratories, including the Beijing Radioactive Ion beam Facility, as well as other scientific platforms at home and abroad. This research covered nuclear theories, numerical models, direct measurements, indirect measurements, and other novel approaches, achieving great interdisciplinary research results, with high-level academic publications and significant international impacts. This article reviews the above research and predicts future developments.

Keywords Nuclear astrophysics · Indirect method · Underground laboratory · Direct measurement · Low-energy nuclear reaction

1 Introduction

Nuclear astrophysics is a field at the intersection of nuclear physics and astrophysics that seeks to understand how all the elements in the Universe were produced and how stars evolve [1]. In astrophysics, various nuclear reactions are crucial to answering basic questions regarding stellar evolution and the origin of elements. These mainly involve reactions induced by neutrons or charged particles, including hydrogen (H), helium (He), and heavy ions such as carbon, neon, and oxygen.

Charged particles involved in reactions are subject to Coulomb repulsion, and the energies corresponding to typical temperatures in stars are significantly below the Coulomb barrier. In a stellar plasma environment, the two-body reaction rate is proportional to an integral involving the product of the Maxwell–Boltzmann factor and Coulomb penetration factor. By differentiating the integrand $e^{-E/kT-2\pi\eta}$ and setting it to zero, the well-known Gamow window can be well defined, in which thermonuclear reactions occur most effectively (see review [2] for details). However, for neutron-induced reactions, there is no Coulomb barrier; thus, the definition of the Gamow window is generally not used. For such reactions, the energy region of interest in astrophysics corresponds simply to the maximum of the Maxwell–Boltzmann distribution, $E = kT$.

Direct measurement of charged particle-induced reactions in the Gamow window is greatly hindered by the vanishing cross section resulting from the small Coulomb barrier penetrability at low energies and competing background reactions. In addition, the rate of cosmic-ray background radiation makes lower-energy direct measurements in laboratories at Earth's surface highly challenging. As an example, the $^{12}C(\alpha, \gamma)^{16}O$ cross section is estimated to be of the order of 10^{-17} b at 300 keV, which corresponds to the typical temperature of He burning. This is approximately several orders of magnitude lower than the sensitivity achieved in the most advanced direct measurements in laboratories on the Earth's surface [2]. In general, these reactions must be measured in laboratories at considerably higher energies; thus, extrapolation down to stellar energies must be performed. However, such extrapolations may lead to significant uncertainties because unknown resonant states often exist in the energy range of astrophysical relevance. For reactions that are extremely difficult, and even impossible, to measure directly, indirect techniques are extremely valuable. These techniques can be used to deduce level parameters (that is, energies, asymptotic normalization coefficients (ANCs) or spectroscopic factors (SFs), and lifetimes), which can then be used in the *R*-matrix or other reaction model analyses [3]. Therefore, several indirect techniques have been developed and applied to date to investigate astrophysical reactions induced by charged particles. Typical indirect techniques include the transfer reaction method [2], ANC method [4], Trojan horse method (THM) [5], Coulomb dissociation (CD) method [6], time-inverse nuclear reaction [7, 8], β-delayed particle emission [9], and elastic α scattering [10]. However, direct measurement is still preferable whenever available because of the limitation of model dependency in indirect methods. The most promising and effective method of revealing clues about stellar evolution would be direct measurement in underground laboratories, such as LUNA [11, 12] (including the LUNA MV facility as a part of the Bellotti Ion Beam Facility [13]), CASPAR [14], JUNA [15–17], and shallow facilities such as those at the Felsenkeller laboratory [18, 19], where the cosmic-ray-induced background is suppressed by several orders of

magnitude, enhancing the sensitivity for cross-section measurement.

Nuclear fusion induced by charged particles above iron is endothermic; thus, it cannot prevent the gravitationally induced collapse of stars. Furthermore, even if it could contribute energetically, the increasing Coulomb barriers with increasing atomic numbers of the constituents in stars would require considerably larger energies to allow fusion to occur. The primary mechanism for producing elements heavier than iron is neutron capture because there are no Coulomb barrier obstacles. Two types of neutron-capture processes are responsible for producing heavy elements: the slow neutron-capture process (known as the *s*-process) and rapid neutron-capture process (known as the *r*-process). Approximately half of elements heavier than iron in the Universe are produced via the *s*-process, which is a series of slow neutron-capture reactions and competing β-decays. During the *s*-process, the neutron number density is relatively low, that is, of the order of 10^7 n cm^{-3}. When the flux reaches an unstable nucleus, it typically decays rather than capturing another neutron, and the *s*-process proceeds via the isotopes around the valley of β-stability [1, 20]. The astrophysical sites of the *s*-process are the burning core He and shell C in massive stars and the "He intershell" of asymptotic giant branch (AGB) stars. The *r*-process is associated with explosive nucleosynthesis in core-collapse supernovae or neutron star mergers. Because of the extremely high neutron densities ($\geq 10^{20}$ cm^{-3}), the timescale for neutron capture is of the order of milliseconds, and the neutron-capture path involves highly neutron-rich nuclei [21]. Direct measurement is extremely difficult and can be impossible because unstable nuclei are often involved during the neutron-capture process, particularly the *r*-process. Therefore, several indirect techniques are extremely valuable and have been developed, such as the transfer reaction [22], surrogate reaction [23], SRM [24], and beta-Oslo methods [25].

In this review, we summarize the recent progress in the investigation of astrophysical reactions and their astrophysical implications at the China Institute of Atomic Energy (CIAE), including direct measurement of astrophysical reactions using the Jinping Underground Nuclear Astrophysics (JUNA) experimental facility (see Sect. 2), direct measurement of the reaction in *p*-process nucleosynthesis using the 1.7-MV tandem accelerator of the CIAE and the 3-MV tandem accelerators of Sichuan University (see Sect. 3), indirect measurement of astrophysical reactions using the CIAE 13-MV tandem accelerator and JAEA 15-MV tandem accelerator (see Sect. 4), measurement of the D(d,n)^{3}He and ^{7}Li(d,n)^{8}Be reactions in laser-induced full plasma (see Sect. 5), and the theoretical study of supernova nucleosynthesis (see Sect. 6), covering future prospects.

2 Direct measurement of astrophysical reactions using the Jinping Underground Nuclear Astrophysics (JUNA) experimental facility

There are now three main deep underground facilities for nuclear astrophysics research: LUNA in Italy, CASPAR in the USA, and JUNA in China. LUNA is the pioneering facility in underground experimental research on nuclear astrophysics and was established in 1991 with the initial installation of a 50-kV accelerator at the Laboratori Nazionali del Gran Sasso (LNGS) of the Italian Istituto Nazionale di Fisica Nucleare (INFN). The 50-kV accelerator was replaced in 2001 with a 400-kV electrostatic machine, which is still in operation today. The LUNA collaboration has successfully established two beamlines, one hosting a windowless gas target system and the other hosting a solid target station. Different combinations of detectors and targets have enabled the LUNA collaboration to extensively study nuclear fusion in different astrophysical environments over the past three decades, including those of the proton–proton (pp) chain, carbon–nitrogen–oxygen (CNO) cycle, and *s*-process [12]. Recently, the LUNA collaboration has successfully installed the LUNA MV facility, with a new batch of experiments proposed [13]. The CASPAR laboratory is the only US-based deep underground accelerator facility, consisting of a 1-MV Van de Graaff-style JN accelerator with an operational range well suited for overlap with higher-energy measurements. The accelerator system has been fully operational since 2018 and is located 4850 feet underground at the Sanford Underground Research Facility (SURF) in Lead, South Dakota, where an overburden with a 4300-m water equivalent (m.w.e.) shielding effect is achieved [14, 26]. The CASPAR laboratory is currently aligned toward the measurement of (α,γ) and (α,n) reactions, such as those in primordial stellar burning reactions and stellar neutron production. The China Jinping Underground Laboratory (CJPL) was established on the site of a hydro-power plant in the Jinping mountain, Sichuan, China [27]. The facility is shielded by 2400 m of mainly marble overburden (6720 m.w.e.) with radioactively quiet rock; thus, the cosmic-ray flux is approximately 100 times lower than that of LUNA. Owing to the advantages provided by the CJPL, the Jinping Underground Nuclear Astrophysics (JUNA) collaboration has proposed to exploit the extremely low background and attempt to reach the Gamow region in CJPL-II A1 Hall [28–33]. CJPL-II A1 Hall was available for temporary usage in year 2020-2021, which allowed the JUNA collaboration to perform the first stage of

experiments (JUNA Run-1). In December 2020, the JUNA collaboration delivered the first accelerator beam underground in CJPL-II A1, and several key astrophysical reactions were then directly measured in the first quarter of 2021, as introduced in subsequent sections. The conditions of three underground experimental platforms are listed in Table 1 [12, 13, 15, 27, 34–38] for reference.

2.1 Accelerators

The JUNA experimental facility features 400-kV electrostatic acceleration and high-intensity ion beams of H^+, He^+, and He^{2+}. In general, the 400-kV accelerator adopts a two-step acceleration and separation mode for JUNA experiments (see Fig. 1). The beams are extracted at a potential of 20–50 kV from a high-intensity electron cyclotron resonance (ECR) ion source and post-accelerated up to 400 keV/q via the acceleration tube.

A 2.45-GHz ECR ion source with a permanent magnet structure has been developed for JUNA to provide H^+ and He^+ beams of several emA for routine operation [34], with a maximum intensity of 10 emA. However, a 2.45-GHz ECR ion source is not capable of producing intense He^{2+} beams. Therefore, a 14.5-GHz permanent magnet high-charge-state ECR ion source was developed to provide He^{2+} beams [39].

Through the development of 2.45-GHz and 14.5-GHz ECR ion sources and high-current beam transmission technology, the JUNA accelerator is capable of delivering 10-emA H^+, 10-emA He^+, and 2-emA He^{2+} beams. Two solenoids are set in the low-energy beam transport (LEBT) system to match the beam to the acceleration tube. Two groups of triple quadrupoles are placed after the tube to match beam transport and meet the requirements of individual experiments. The inhibition of beam impurities is achieved by two dipoles. One is on the 400-kV high-voltage platform (30°), and the other is on the ground potential (90°). The beam transmission efficiency is higher than 90%, and the long-term stability of the beam energy is better than 0.05%. To calibrate the energy of the accelerator and the stoichiometry of the target, a typical proton beam was used to scan the resonance yield curves in known reactions. The benchmark resonances for the calibration originated from results reported in previous direct measurements. A typical uncertainty is approximately 1.1 keV for $E_{\mathrm{beam}} = 474.0$ keV (see, for example, [40] for details). The condition of high beam intensity provides great advantages for JUNA in conducting research in the field of nuclear astrophysics.

2.2 Detectors and targets

JUNA developed a high-efficiency BGO array and ^{3}He tube array for gamma and neutron detection, respectively. Using low-background materials, integrated detection and shielding systems with a multilayer structure were established. The BGO array consists of eight BGO crystals, with each individual block occupying approximately 45° in the Φ direction. The neutron detection array consists of 24 ^{3}He-filled proportional counters embedded in a polyethylene matrix. A 7% borated polyethylene layer was wrapped around the detection array to shield against environmental neutrons. Moreover, a waveform identification method for neutron detection and a flash number screening program for gamma detection were developed to further suppress the experimental background. The background levels of the JUNA detection arrays have been tested and are listed in Table 2 [41–43].

A mA-level high-power target was developed via surface microchannel water cooling. Furthermore, using a high-purity substrate combined with ion implantation, surface plating, and filtered cathodic vacuum arc (FCVA)

Table 1 Conditions for the LUNA (including LUNA 400 kV and LUNA MV), CASPAR, and JUNA experimental platforms

	Muon flux ($cm^{-2}s^{-1}$)	Beam energy (keV)			Beam current (emA)		
		$^1H^+$ $^{12,13}C^+$	$^4He^+$ $^{12,13}C^{2+}$	$^4He^{2+}$	$^1H^+$ $^{12,13}C^+$	$^4He^+$ $^{12,13}C^{2+}$	$^4He^{2+}$
LUNA 400 kV [12, 35]	3.2×10^{-8}	50–400	50–400	–	≤ 1.0	≤ 0.5	–
		–	–		–	–	
LUNA MV [13, 36]	–	300–3500	300–3500	–	≤ 1.0	≤ 0.5	–
		300–3500	600–7000		≤ 0.15	≤ 0.1	
CASPAR [37, 38]	4.4×10^{-9}	150–1100	150–1100	–	≤ 0.25	≤ 0.25	–
		–	–		–	–	
JUNA 400 kV [15, 27, 34]	2.0×10^{-10}	50–400	50–400	100–800	≤ 10	≤ 10	≤ 2
		–	–		–	–	

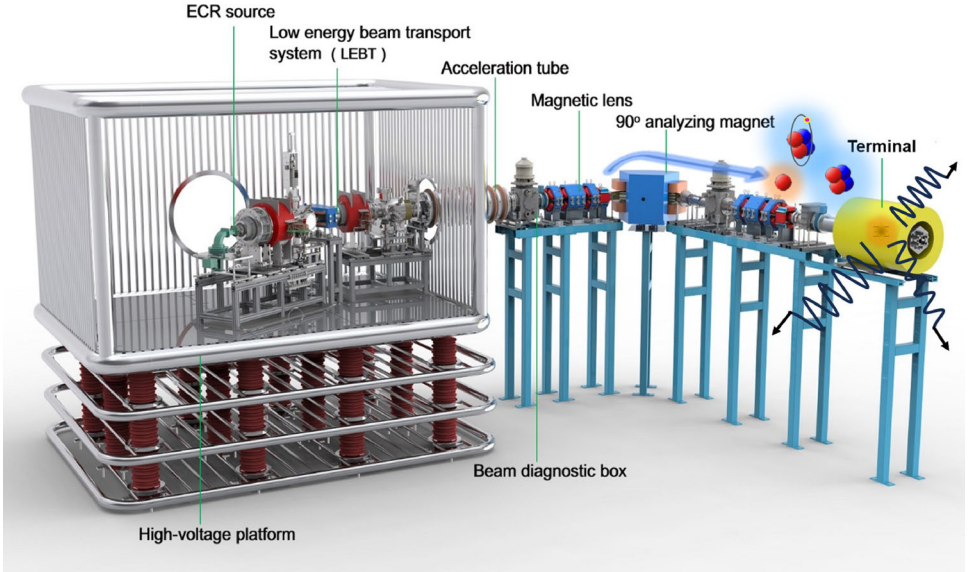

Fig. 1 (Color online) Complete side view of the JUNA 400-kV accelerator and Run-1 detection terminal. JUNA 400-kV can now provide high-intensity H^+, He^+, and He^{2+} beams

Table 2 Typical detector background level in JUNA Run-1. Note that the highest energy γ-ray from the common natural radioactive background is 2.6 MeV, originating from the decay of ^{208}Tl. Therefore, the background above 3 MeV arises mainly from the cosmic-ray-induced background. The most significant effect of background reduction can be found for $E \geq 3$ MeV in an underground laboratory. The higher the energy ($E \leq 10$ MeV), the more significant the shielding effect. For example, there is only negligible count for $E \geq 8$ MeV (see Fig. 4 in [41] for details). This is why there is an order of magnitude between the count rate of the 4–6 MeV and 6–10 MeV ranges in the BGO

Detector type	Background count rate		
	Energy range (MeV)	Ground	CJPL (A1-Hall)
BGO array [41]	4–6	2.35 $keV^{-1}h^{-1}$	3.1×10^{-3} $keV^{-1}h^{-1}$
	6–10	1.52 $keV^{-1}h^{-1}$	1.4×10^{-4} $keV^{-1}h^{-1}$
^{3}He neutron detector [42, 43]	–	1238 h^{-1}	4.7 h^{-1}

technologies, a high-purity isotope-enriched target was prepared, which can solve various surface-effect problems caused by high-current beams (for example, see [44–47] for details). Under strong irradiation conditions, the stability of such a target can be maintained without significant loss of thickness; hence, there is no need to frequently replace the target during long-term experiments. Combined with the advantage of high-intensity beams, data can be collected more effectively.

High-efficiency detector arrays and radiation-resistant targets, along with a cold trap to minimize carbon build-up on the target surface, a ring electrode applied with a negative voltage to suppress secondary electrons, and several apertures, constitute the detection terminal of the JUNA platform, as shown in Fig. 2. Note that Fig. 2 provides a general impression of the detection terminal, considering that the detection terminals used in JUNA Run-1 experiments are similar. The setup details of each experiment can be found in specific published articles.

Using the equipment described above, five groups of key astrophysical reactions were studied during JUNA Run-1. Some research results and highlights are presented in the following sections.

2.3 JUNA Run-1 experiment results and achievements

In the JUNA Run-1 campaign, $^{12}C(\alpha,\gamma)^{16}O$, $^{13}C(\alpha,n)^{16}O$, $^{18}O(\alpha,\gamma)^{22}Ne$, $^{19}F(p,\gamma)^{20}Ne$, $^{19}F(p,\alpha\ \gamma)^{16}O$, $^{25}Mg(p,\gamma)^{26}Al$, and other reactions were measured with a high-intensity beam and high-efficiency detectors. The basic parameters are listed in Table 3 [40, 43, 48–50]. The results and their impact on astrophysics are discussed below in detail.

2.3.1 $^{12}C(\alpha,\gamma)^{16}O$

The $^{12}C(\alpha,\gamma)^{16}O$ reaction (also called the holy grail reaction), together with the 3α process, determines the absolute abundance of carbon and oxygen, which is the

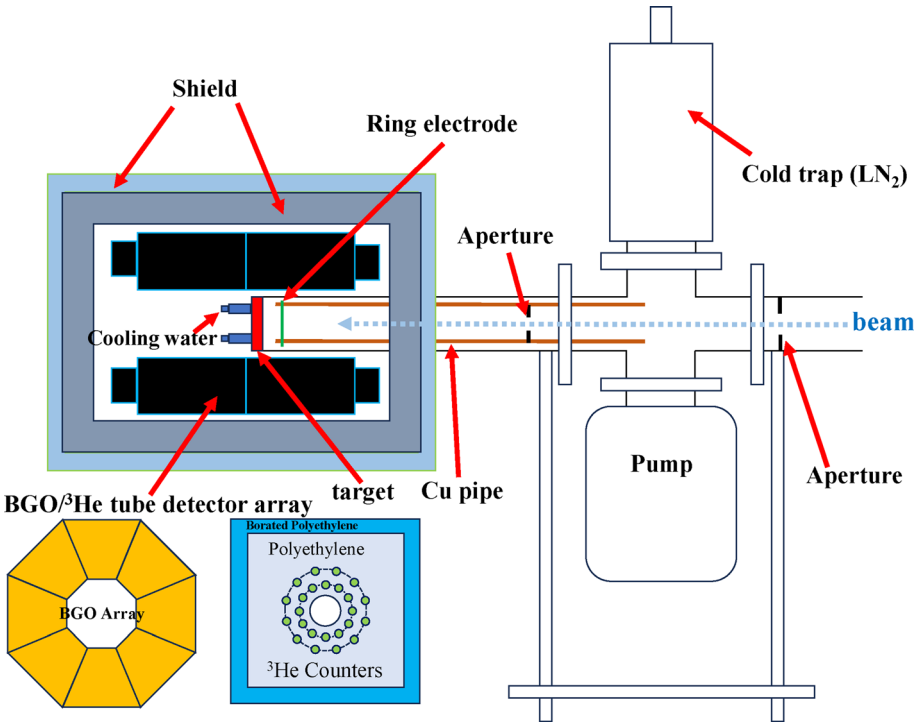

Fig. 2 (Color online) Schematic of the JUNA Run-1 detection terminal

Table 3 Beam conditions for the first batch of JUNA experiments

Experiment	Parameters			
	Beam	Beam energy (keV)	Current (emA)	Beam exposure (C)
$^{12}C(\alpha,\gamma)^{16}O$	He^{2+}	740–820	1	400
$^{13}C(\alpha,n)^{16}O$ [43]	He^{2+}	400–785	0.3	12.4
	He^{+}	300–400	0.5−2.5	363
$^{18}O(\alpha,\gamma)^{22}Ne$ [40]	He^{2+}	470–787	1	120
$^{19}F(p,\alpha\ \gamma)^{16}O$[48]	H^{+}	76–362	1	475
$^{19}F(p,\gamma)^{20}Ne$[49]	H^{+}	195–350	1	40
$^{25}Mg(p,\gamma)^{26}Al$ [50]	H^{+}	110	2	1400

fundamental basis for all organic chemistry and the evolution of biological life in our Universe [3, 51, 52]. The carbon–oxygen ratio at the end of He burning affects not only the production of all elements heavier than $A = 16$, but also the explosion of supernovae. Additionally, according to stellar evolution theory, the black hole (BH) mass gap depends sensitively on the $^{12}C(\alpha,\gamma)^{16}O$ reaction rate, because it influences the ratio of carbon and oxygen at the end of the core He burning stage and impacts the final fate of massive stars [53, 54]. This demonstrates another strong motivation for precise determination of the $^{12}C(\alpha,\gamma)^{16}O$ reaction rate.

Significant efforts have been made in the past several decades to further our understanding of this fundamental reaction; however, most estimates remain far from the 10% maximum uncertainty required by stellar models [51, 55]. Numerous direct measurement experiments have been conducted in laboratories on the Earth's surface [56–70], achieving a lowest energy of $E_{c.m.}$ = 891 keV [56–58] because of the extremely low cross section resulting from the small Coulomb penetrability at low energies and the high cosmic-ray-induced background at γ-ray energies greater than 3 MeV.

In current JUNA research, the $^{12}C(\alpha,\gamma)^{16}O$ was directly measured at $E_{c.m.}$ = 552 keV with a 1-emA $^{4}He^{2+}$ beam. The $^{4}He^{2+}$ beam provided by the JUNA accelerator was directed by two collimators and then bombarded on a 99.99% ^{12}C-enriched ion-deposited titanium carbon target with a thickness of more than 1 μm [44], which was cooled by flushing the back of the target with water. The γ-rays emitted from the target were measured by the JUNA 4π BGO array. A lanthanum(III) bromide ($LaBr_3(Ce)$) detector was placed close to the target to cover more solid angles and also act as an anti-coincidence detector. A variety of

methods were employed to suppress the beam-induced and natural γ/neutron backgrounds. The collimators were coated with a layer of high-purity tantalum to prevent unwanted reactions with impurities during beam transfer. The BGO array was shielded by 5-mm Cu, 100-mm Pb, and 1-mm Cd layers.

Because the 7.7-MeV gamma rays of $^{12}C(\alpha,\gamma)^{16}O$ directly decay to the ground state (g.s.) in ^{16}O, the multiplicity of the BGO array signal was selected to suppress the cascading gamma background induced by neutrons and other (α,γ) and (p,γ) reactions. According to a test with an Am-Be neutron source, the neutron-induced gammas within 7000–8000 keV could be suppressed by a factor of four with the current anti-coincidence setup. Moreover, Compton scattering gammas from higher energies could be suppressed. The efficiency of the 7.7-MeV gamma rays from $^{12}C(\alpha,\gamma)^{16}O$ with the anti-coincidence setup was determined to be 17.7%, which is approximately 0.6 times the total summing efficiency (30.5%).

The data are now under careful processing, and we have so far identified the signal from $^{12}C(\alpha,\gamma)^{16}O$ with a confidence level of approximately 1σ. The results will be finalized and published in the near future.

2.3.2 $^{13}C(\alpha,n)^{16}O$

The $^{13}C(\alpha,n)^{16}O$ reaction was the first neutron source used in the stellar models proposed by Cameron and Greenstein in 1954. This reaction produces neutrons for the main *s*-process in AGB stars, which synthesize nearly one half of elements heavier than iron in the Universe [20, 71, 72]. It may also be activated in metal-poor stars to supply neutrons for intermediate neutron-capture process (*i*-process) nucleosynthesis [73–77]. Precise determination of the reaction cross section is needed at associated Gamow windows of approximately $E_{c.m.}$ = 0.15−0.3 MeV and 0.2−0.54 MeV to accurately predict the neutron density and final isotopic abundances from stellar models. Limited by the cosmic background in laboratories on the Earth's surface, direct measurement was ceased at energies above $E_{c.m.}$ = 0.27 MeV, with an error bar of approximately 60%, for being unable to effectively constrain the crucial threshold state and provide a reliable extrapolation down to stellar energies.

A recent breakthrough in the direct measurement of this reaction was reported by the LUNA collaboration at $E_{c.m.}$ = 0.23−0.30 MeV, that is, the upper range of the *s*-process Gamow window [78]. However, for the extrapolation of the *S*-factor to low energies, they had to rely on other measurements at higher energies, which revealed inconsistencies (see text in [43] for details). As a result, their recommended reaction rate has a large uncertainty, leading to sizeable variations in the predictions of several important isotopes such as ^{60}Fe and ^{205}Pb in the AGB model.

In JUNA research, a direct measurement of the $^{13}C(\alpha,n)^{16}O$ reaction cross section was conducted over the range of $E_{c.m.}$ = 0.24−1.9 MeV at underground (CJPL) and above-ground (Sichuan University, SCU) laboratories, with the highest precision to date [43]. The underground experiment was performed at $E_{c.m.}$ = 0.24−0.59 MeV using the most intense beam available in deep underground laboratories. The above-ground measurement was performed with the same detection setup in the range of $E_{c.m.}$ = 0.75–1.9 MeV using the $^4He^+$ beam at the 3-MV Tandetron at Sichuan University to resolve the discrepancies among previous direct measurements at higher energies. Furthermore, 2-mm-thick ^{13}C-enriched targets with a purity of 97% were used to avoid the source of systematic uncertainty incurred by target deterioration in traditional thin-target experiments. The thick targets were highly stable, and only two targets were used for the entire experiment. At Sichuan University, the same detection setup was used to minimize additional systematic uncertainties in both thick-target and thin-target measurements.

The measurement provides self-consistent calibration of neutron detector efficiency, covers almost the entire *i*-process Gamow window, in which the large uncertainty of previous experiments was reduced from 60 to 15%, and eliminates the large systematic uncertainty in extrapolation arising from the inconsistency of existing datasets. Finally, the JUNA research provides a more reliable reaction rate for the study of the *s*- and *i*-processes, as well as the first direct determination of the alpha strength for the near-threshold state. The *S*-factor and corresponding best fit are shown in Fig. 3, revealing the importance of obtaining self-consistent data within a wide energy range. Future stellar models based on the next generation of multi-dimensional hydrodynamics simulations will be more predictive owing to the more reliable reaction rates provided by JUNA research.

2.3.3 $^{18}O(\alpha,\gamma)^{22}Ne$

According to classical AGB theory, convection first occurs between the H and He shells, then the H-rich material enters the He shell, and ^{12}C, the product of He burning, forms a "pocket" composed of ^{13}C. The $^{13}C(\alpha,n)^{16}O$ reaction is subsequently activated, which produces the main neutron flux for the *s*-process (see also the discussion on the $^{13}C(\alpha,n)^{16}O$ reaction above). This reaction is the main neutron source of low- or medium-mass AGB stars. In more massive AGB stars, the temperature becomes higher, and the $^{22}Ne(\alpha,n)^{25}Mg$ reaction is activated, which plays an essential role in the weak

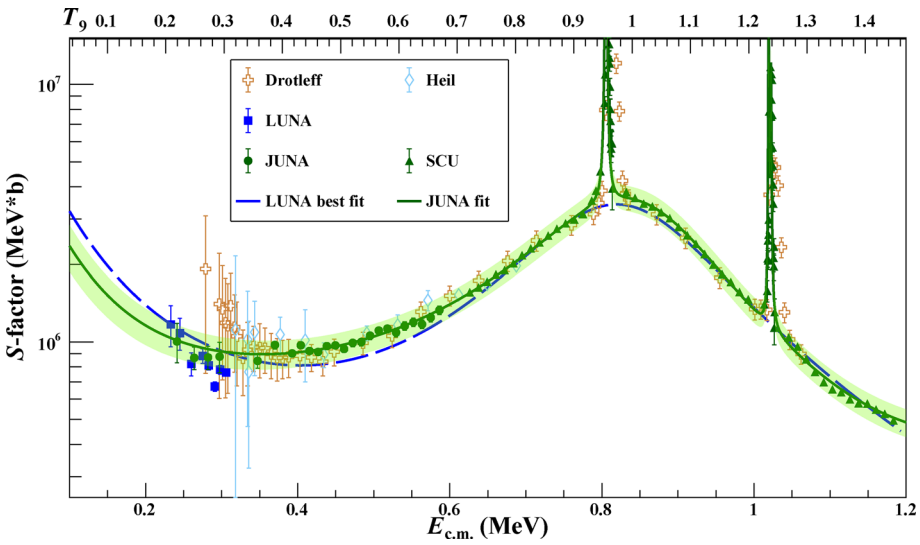

Fig. 3 (Color online) *S*-factor of the $^{13}C(\alpha,n)^{16}O$ reaction. The best fit and corresponding uncertainty recommended by JUNA (with both JUNA and SCU data) are shown as green solid lines and a green shaded band, respectively. The *S*-factors were corrected with the screening potential U_e = 0.78 keV. The measurement provides self-consistent data in a wide energy range and greatly reduces the large uncertainties of previous experiments [43]. The temperatures in T_9 on the top correspond to the central energy of the Gamow window on the bottom

component of the *s*-process [20, 71, 72, 79, 80]. ^{22}Ne is mainly produced via the $^{14}N(\alpha,\gamma)^{18}F(\beta^+,\nu)^{18}O(\alpha,\gamma)^{22}Ne$ chain. Therefore, the production of neutrons from the $^{22}Ne(\alpha,n)^{25}Mg$ reaction relies heavily on the front $^{18}O(\alpha,\gamma)^{22}Ne$ reaction rate. In addition, the $^{18}O(\alpha,\gamma)^{22}Ne$ reaction also determines the abundance ratio of neon isotopes synthesized in AGB stars. Because $^{21}Ne/^{22}Ne$ can be constrained from the analysis of the SiC grains of meteoritic stardust originating from AGB stars with high precision [81], the comparison between model predictions and observational constraints helps reveal the mass of parent AGB stars. In the energy range of interest (T $\sim$ 0.1−0.3 GK), the $^{18}O(\alpha,\gamma)^{22}Ne$ resonances that dominate the reaction rate occur near E_α = 470 and 660 keV. However, the former is weak and thus cannot easily be directly investigated at above-ground laboratories. The most recent attempt at this was the first direct measurement of the total resonance strength of the 470-keV resonance by CASPAR [82]. However, only two previous experiments, $^{18}O(^6Li,d)^{22}Ne$ and $^{20}Ne(t,p)^{22}Ne$, have used indirect transfer reactions to determine the resonance energy, 470 ± 18 keV and 495 ± 12 keV, respectively (see references and discussion in [40]). The lack of a reported precise resonance energies persistently introduces substantial uncertainties to the $^{18}O(\alpha,\gamma)^{22}Ne$ reaction rate.

JUNA determined the resonance energy to be E_α = 474.0 ± 1.1 keV (see Fig. 4) by scanning the yield curve via both direct measurement and with the highest precision for the first time. In the JUNA research, ^{18}O-enriched gas was used to produce $Ti^{18}O_x$ (where *x* is the atomic ratio of oxygen to titanium) targets through FCVA technology. The degradation of the target was measured to be 6% after 94 Coulomb $^4He^{2+}$ irradiation by monitoring the maximum yield of the 660-keV resonance.

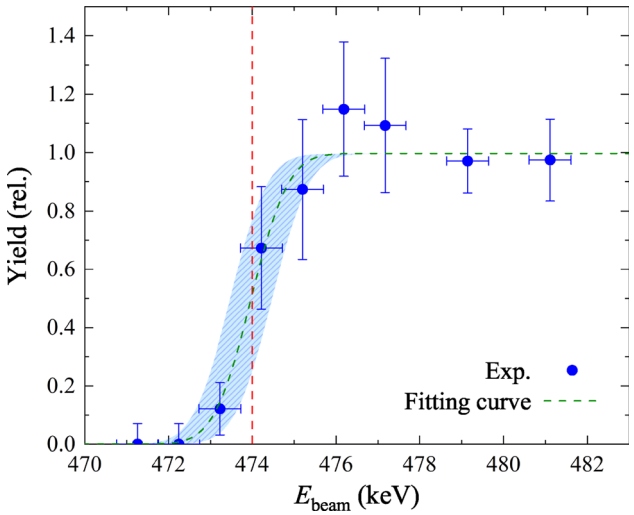

Fig. 4 (Color online) Thick-target yield curve of the 470-keV resonance in $^{18}O(\alpha,\gamma)^{22}Ne$. The lateral error represents the energy uncertainty of beams, and the vertical error represents the yield uncertainty. The dashed green line is the fitting curve, the blue shadow represents the uncertainty of the fitting curve, and the dashed red line marks the position of resonance energy [40]

Via the above efforts, the precision of the $^{18}O(\alpha,\gamma)^{22}Ne$ reaction rates was improved by up to approximately 10 times. The new reaction rates have allowed us to provide more accurate and precise predictions of $^{21}Ne/^{22}Ne$ abundances in the intershell of AGB stars, improving the possibility of probing the origin of stardust SiC grains of different sizes (see Fig. 5)[40].

2.3.4 $^{19}F(p,\alpha\,\gamma)^{16}O$ & $^{19}F(p,\gamma)^{20}Ne$

Fluorine nucleosynthesis is an open issue in modern astrophysics. In 1988, shortly after the discovery of SN1987, Woosley & Haxton [83] proposed fluorine

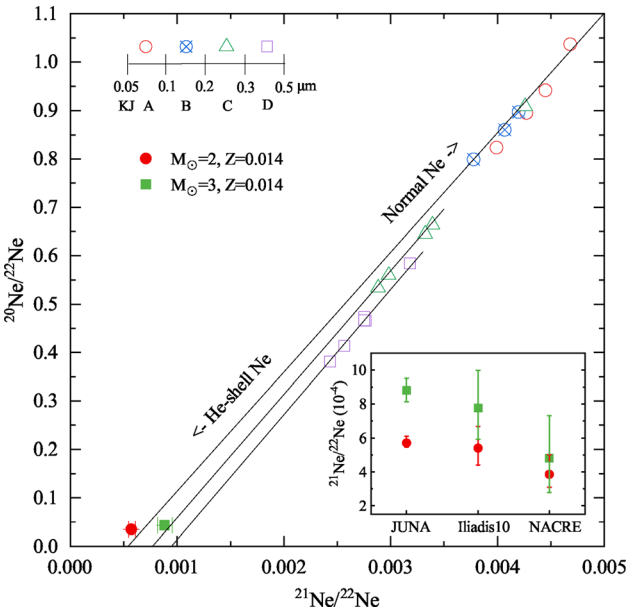

Fig. 5 (Color online) Ne isotopic ratios predicted in the intershell of different AGB models (filled symbols) using the JUNA $^{18}O(\alpha,\gamma)^{22}Ne$ reaction rates and those observed in meteoritic stardust SiC grains of different sizes [81] (open symbols). The symbol legend is shown at the top-left of the plot. The three regression lines denote fits to the KJB, KJC, and KJD samples, representing the mixing between a material of normal composition (≈solar, located at the top-right outside the plot boundaries) and AGB He-shell composition (located at the bottom left). The bottom-right inset shows the $^{21}Ne/^{22}Ne$ ratios calculated with different $^{18}O(\alpha,\gamma)^{22}Ne$ reaction rates. See [40] for further details

production in Type II core-collapse supernovae (SNe) via neutrino spallation on ^{20}Ne nuclei. However, no fluorine spectrum has been observed in supernova remnants. In 1992, Jorissen et al. [84] observed HF lines from stars outside the solar system for the first time, providing evidence of fluorine production during shell-He burning in AGB stars. However, the observed fluorine abundance was considerably higher than the standard AGB model prediction, and additional mixing was still required [85]. This is the so-called fluorine overabundance problem. Although several other possible production sites were also investigated [86, 87], it remains unclear how each contributes to the observed fluorine abundance.

Precise $^{19}F(p,\alpha)^{16}O$ reaction rates may play an essential role in solving this problem because fluorine and H are consumed at the same time and fluorine surface abundances may be modified [85, 88–91]. At the current temperature region of astrophysical interest (0.1−0.3 GK), the corresponding Gamow window is located at $E_{c.m.} \approx 70$–350 keV. In this energy region, the $^{19}F(p,\alpha)^{16}O$ reaction is dominated by the (p,α_0) and $(p,\alpha\,\gamma)$ channel. Previously, the $(p,\alpha\,\gamma)$ channel was measured down to $E_{c.m.} \approx 189$ keV at an above-ground laboratory [92], which is still far from the lower edge of the Gamow window.

JUNA measured the $^{19}F(p,\alpha\,\gamma)^{16}O$ channel down to the lowest energy of $E_{c.m.} \approx 72$ keV [48, 93], and the energy region under investigation fully covered the Gamow window of AGB stars relevant to fluorine production. The ^{19}F implanted targets [46, 47] exhibited a material loss of less than 7% under $\sim$ 200 C bombardment. Our new JUNA rate deviates significantly from the previous expectations [94] by a factor of 0.2−1.3 [48]. Together with the previous (p,α_0) data, the JUNA research provides strong experimental evidence that the total $^{19}F(p,\alpha)^{16}O$ rate is dominated by the (p,α_0) channel at the low temperature region of 0.03−0.12 GK. Therefore, precise direct (p,α_0) measurement is required in the future.

In addition, as a breakout reaction from the CNO cycle, the $^{19}F(p,\gamma)^{20}Ne$ reaction competes with $^{19}F(p,\alpha)^{16}O$ and affects the $(p,\gamma)/(p,\alpha)$ rate ratio (see Fig. 6a). Previously, this reaction was thought to be weak compared to the $^{19}F(p,\alpha)^{16}O$ reaction; therefore, most of the ^{19}F produced by the CNO cycle would be recycled back into ^{16}O, with no substantial changes in chemical abundance. JUNA measured the $^{19}F(p,\gamma)^{20}Ne$ reaction down to a low-energy point of 186 keV, reporting a key resonance at 225 keV [49]. This surprising resonance highlighted the origin of the anomalous calcium abundance observed in SMSS0313-6708, one of the oldest known stars (an ultra-metal-poor star), as suggested by a mechanism proposed to explain the chemical abundances measured in this early star. In this mechanism, after light metals such as carbon and oxygen are created, and early in the star's evolution, subsequent follow-up proton and/or neutron-capture reactions generate an abundance of heavier elements up to calcium. Based on the JUNA results, the $^{19}F(p,\gamma)^{20}Ne$ reaction rate of population III stars could be 7.4 times higher than previous estimates. Therefore, the JUNA results may explain the high calcium content of SMSS0313-6708 (see Fig. 6b), which represents a significant achievement in interpreting astrophysical puzzles from the perspective of nuclear physics.

2.3.5 $^{25}Mg(p,\gamma)^{26}Al$

The HEAO-3 satellite was the first to observe 1809-keV γ-rays emitted by ^{26}Al β decay [95, 96], marking the advent of the era of γ-ray astronomy. Subsequently, considerable efforts in γ-ray astronomy (for example, see Refs. [97–99]) have revealed the mass and distributions of ^{26}Al in the Galaxy. This discovery revealed that ^{26}Al nucleosynthesis is still active in our Galaxy because the half-life of the ^{26}Al g.s. is only 0.72 million years, which is significantly shorter than the age of our Galaxy.

The $^{25}Mg(p,\gamma)^{26}Al$ reaction is the primary pathway to producing ^{26}Al in several candidate astrophysical sites (for

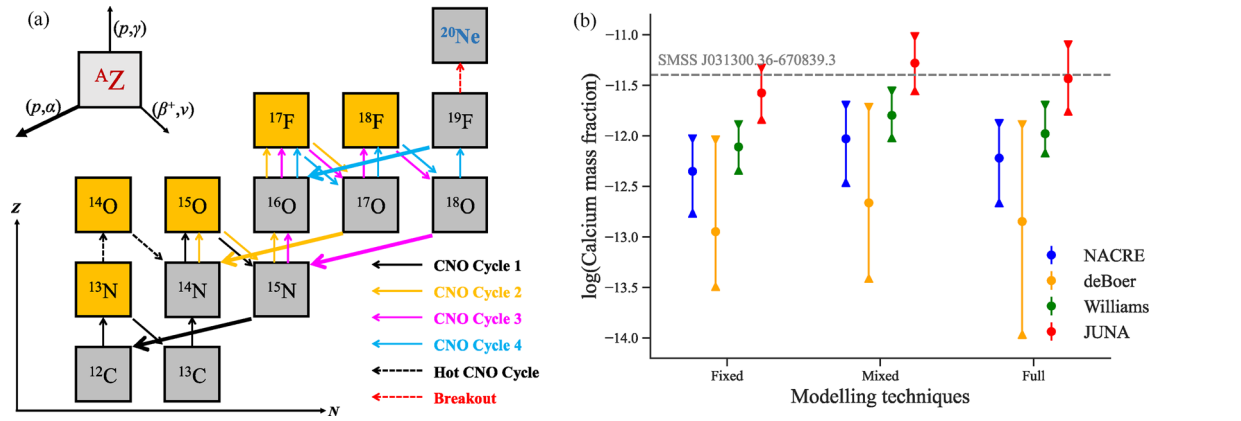

Fig. 6 (Color online) Calcium abundance predicted for SMSS0313-6708 based on different datasets (left panel) and CNO cycles (right panel)[49]

example, AGB stars [100], Wolf-Rayet stars [101], O-Ne-Mg nova [102], and core-collapse supernovae [103]), and its reaction rates are dominated by the resonant capture reactions of several low-energy resonances in the range of $E_{\mathrm{c.m.}}$ = 30–400 keV (at astrophysical temperatures below 0.2 GK). Many experiments have been performed since 1970; however, direct measurements in above-ground laboratories can only reach a resonance of 189 keV. In 2012, LUNA measured the resonance strength of ^{25}Mg$(p,\gamma)^{26}$Al at 92 keV in pioneering work [104, 105]. However, their results produced significant uncertainties for both the resonance strength and ground-state feeding factor owing to the relatively low beam intensity.

In JUNA research, the low-energy $E_{\mathrm{c.m.}}$ = 92, 130, and 189-keV resonances of the ^{25}Mg$(p,\gamma)^{26}$Al reaction were directly measured using a proton beam up to 2 emA, with the thicknesses of the ^{25}Mg isotopic targets set to approximately 60 μg/cm^2. The resonance strength $\omega\gamma$ and ground-state feeding factor were determined to be $(3.8 \pm 0.3) \times 10^{-10}$ eV and 0.66 ± 0.04, respectively. The JUNA results significantly reduced the uncertainties of the reaction rates at temperatures of 0.05−0.15 GK (see Fig. 7) and provided the ground-state feeding factor to the highest precision, that is, 0.66 ± 0.04, with at least a factor of 2 in uncertainty reduction when compared to the 12–33% relative uncertainty in previous studies (see text in [50]) for details. The recommended new ^{25}Mg$(p,\gamma)^{26}$Al reaction rates are a factor of 2.4 larger than those adopted in the REACLIB database at a temperature of around 0.1 GK. The new results indicate higher production rates for the ^{26}Al g.s. as well as cosmic 1.809-MeV γ-rays. The precise reaction rates from this research will provide an effective constraint for the study of the convection model in AGB stars and offer further support to explain the observed distribution of magnesium isotopes and the overall Mg-Al trend in stars such as M13 and NGC 6752.

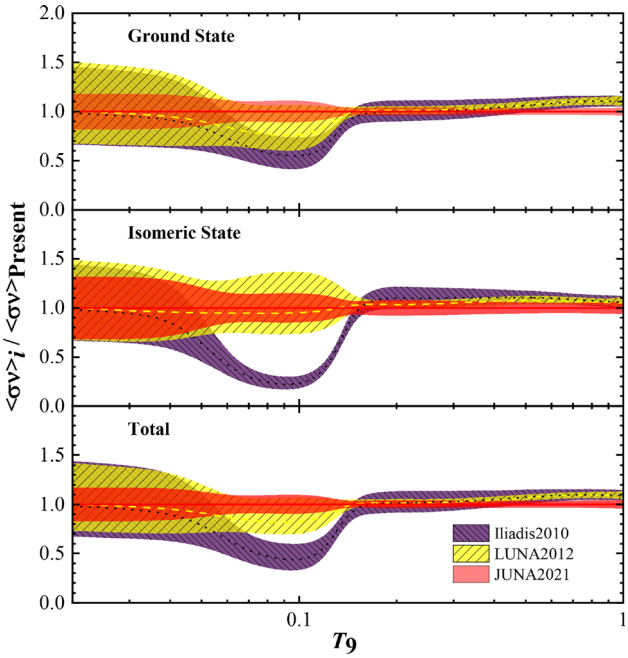

Fig. 7 (Color online) Comparison between the JUNA ^{25}Mg$(p,\gamma)^{26}$Al reaction rates [50], the LUNA results(yellow-dashed line) [105], and those adopted in REACLIB (blue dotted line). The red shaded, yellow backslash, and dark violet areas represent the 1σ uncertainties of the present and other research

3 Direct measurement of the ^{74}Ge$(p,\gamma)^{75}$As reaction in *p*-process nucleosynthesis using the 1.7-MV tandem accelerator of the CIAE and the 3-MV tandem accelerators of Sichuan University

For the lightest *p*-nuclei ^{74}Se, the prediction of stellar models is approximately three times higher than the solar abundance [106]. According to sensitivity studies [106, 107], the ^{74}Se isotope is mainly produced via the reaction chain ^{74}Ge$(p,\gamma)^{75}$As$(p,n)^{75}$Se$(\gamma,n)^{74}$Se, and

^{74}Se(γ,α)^{70}Ge is the main destruction reaction. ^{74}Ge(p,γ)^{75}As was the remaining reaction used to explore ^{75}As production [108] and was suggested to have a direct impact on this production [106].

The Gamow window for the ^{74}Ge(p,γ)^{75}As reaction in typical stellar environments is E_p = 1.2−3.7 MeV. Therefore, two accelerators at different energies were used in our experiments to better span this energy range. A low-energy-area experiment at E_p = 1.4−2.8 MeV was performed at the 1.7-MV tandem accelerator of the CIAE [109], and the 3-MV tandem accelerator of Sichuan University (SCU) was used to measure the reaction cross sections at E_p = 2.5−4.3 MeV via in-beam γ spectroscopy [110]. Four high-purity germanium (HPGe) detectors were closely mounted at different angles to measure the intensities and angular distributions of the prompt γ rays of ^{74}Ge(p,γ)^{75}As reactions. A typical in-beam spectrum at a beam energy of 2.8 MeV at 108° is shown in Fig. 8. For the γ_0 transition from the entry to g.s., the energy was determined using $E_\gamma = E_{c.m.} + Q$, where $E_{c.m.}$ is the center-of-mass energy, and Q = 6900.72 ± 0.88 keV is the Q value of the ^{74}Ge(p, γ)^{75}As reaction. The deexcitation recoil energy of the γ_0 transition was negligible, and the maximum Doppler shift was 17.3−63.4 keV for E_p = 1.4−4.3 MeV. γ ray energies can be higher than 11 MeV; therefore, the ^{27}Al(p,γ)^{28}Si resonance reactions at E_p = 992 keV and E_p = 1800 keV with the highest γ energy of 13321 keV [111] were used to calibrate the high-energy efficiencies of the HPGe detectors.

The reaction cross sections were determined using the total γ transitions to the g.s. from 35 excited states and the entry state. The measured cross sections of the ^{74}Ge(p,γ)^{75}As reaction are shown in Fig. 9, along with a comparison of previous experiments [108, 112]. The present results are in good agreement with the previously available data and extend the measurement to lower and higher energies. The difference between the cross section at E_p = 1.4 MeV and the theoretical values given by Ref. [108] increased to 160%. The EMPIRE code was used with the KD global optical potential and different level densities to perform new theoretical calculations to better describe the experimental cross sections of the ^{74}Ge(p,γ)^{75}As reaction, the results of which are also shown in Fig. 9. As shown, the EMPIRE-EGSM calculation best described the

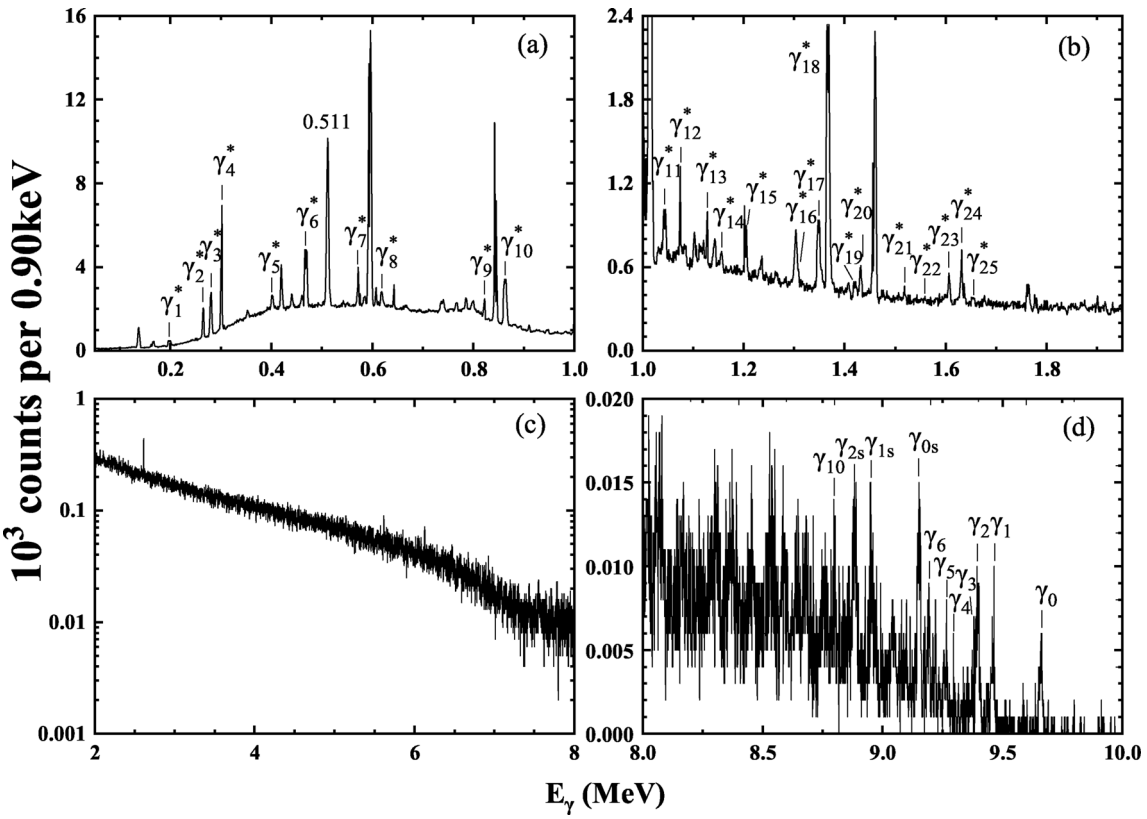

Fig. 8 Typical spectrum of the ^{74}Ge(p,γ)^{75}As reaction for E_p = 2.8 MeV at 108°. Transitions to the g.s. of the reaction product ^{75}As are marked with the label $*$. In particular, the transition from the entry state to g.s. is denoted by γ_0, whereas the transition to the first excited state is denoted by γ_1, and so on. Several single escape peaks of these transitions are also marked with *s*. Some peaks are not marked in the figure owing to their relatively low counts, which require additional figures to present in detail [109]

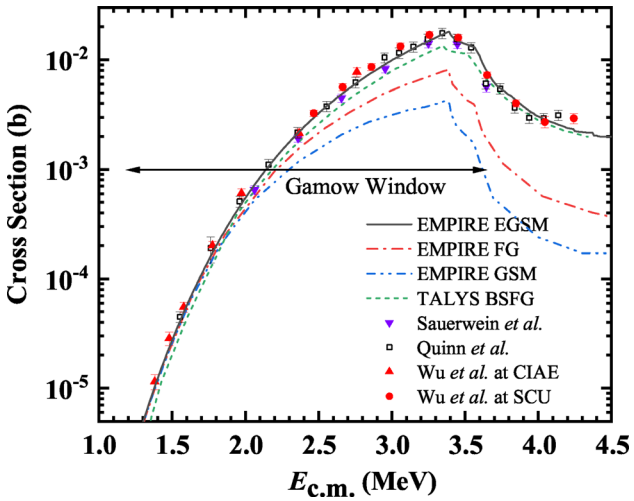

Fig. 9 (Color online) Experimental cross sections of the ^{74}Ge(p,γ)^{75}As reaction compared with those of current studies and theoretical calculations [110]

experimental data, especially at low energies. New reaction rates were extracted using the EMPIRE-EGSM calculation. Ratios of the new reaction rates to those of previous studies and the REACLIB compilation are shown in Fig. 10. In the temperature range 1.8−3.3 GK relevant to p-process nucleosynthesis, the new reaction rates were higher than those of Ref. [112], with a maximum increase of 20%, higher than those of Ref. [108], with a maximum increase of 18%, and higher than those of the REACLIB compilation, with a maximum increase of 47%. Our studies worsened the previous overproduction of ^{74}Se compared to the observed abundance.

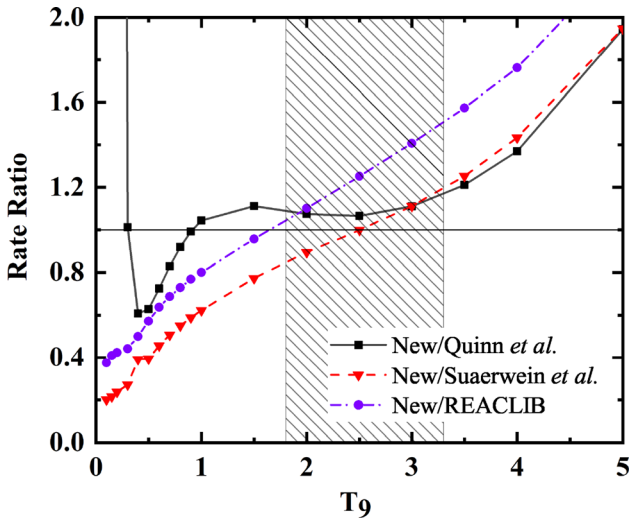

Fig. 10 (Color online) Ratios of the new reaction rates to the previous values and REACLIB compilation. The shaded area represents the temperature range 1.8−3.3 GK for the p-process [110]

4 Indirect measurement of astrophysical reactions using the CIAE 13-MV tandem accelerator and JAEA 15-MV tandem accelerator

In some cases, direct measurement is extremely difficult in explosive burning or astrophysical r-process scenarios, where neutron or unstable isotope targets cannot be fabricated. In other cases, under-threshold resonances are important but cannot be measured directly. Indirect reactions, which often involve single-nucleon or cluster transfer the same as that of direct ones, can sometimes overcome these difficulties and provide a significant improvement in cross section by many orders of magnitude [113]. Therefore, indirect techniques are highly valuable and have been developed in various forms, such as the transfer reaction method [22], SRM [24], thick-target inverse kinematics method [114], THM [5], and CD method [6]. Because the scope of this review is limited to activities at the CIAE, we focus on the progress in some of the methods mentioned above.

4.1 Indirect measurement of the ^{12}C(α,γ)^{16}O reaction with the ANC method

The cross section of the ^{12}C(α,γ)^{16}O reaction is extremely small in the Gamow window, which makes direct measurements difficult in ground-based laboratories. Indirect methods can determine the level parameters and achieve reliable extrapolations of the cross section from higher energies to the Gamow window through the phenomenological R matrix method [3]. The two main capture modes in the ^{12}C(α,γ)^{16}O reaction are the $E1$ and $E2$ g.s. transitions. The $E2$ transition to the g.s. mainly includes external capture to the ^{16}O g.s. and the subthreshold 2^+ resonance at E_x = 6.917 MeV. The $E1$ transition to the g.s. includes the low-energy tail of the broad 1^- resonance at E_x = 9.585 MeV and the subthreshold 1^- resonance at E_x = 7.117 MeV. The measurement of these two subthreshold states of ^{16}O is the focus of indirect experiments.

The α-cluster transfer reaction is an important indirect method of studying the holy grail reaction [2]. Owing to its spin and isospin symmetry, and hence its high binding energy, an α-cluster can propagate within a nucleus relatively unperturbed for a significant amount of time [115]. α-clusters can preferentially populate natural-parity isoscalar states. By measuring the angular distributions of the α-cluster transfer induced by light nuclei, astrophysical reaction cross sections can be studied at higher energies than the Gamow window.

We performed a series measurements of ^{12}C(^{11}B, ^{7}Li)^{16}O reactions to determine the ANCs and S factors of the ^{12}C(α, γ)^{16}O reaction. The experiments were

conducted at the HI-13 tandem accelerator national laboratory of the CIAE [116–118]. The setup of the experiments is shown in Fig. 11 (an introduction to the Q3D spectrometer can be found in [119]). A 50-MeV ^{11}B beam was directed onto a natural carbon self-supported target to measure the angular distribution of the ^{12}C(^{11}B,^{7}Li)^{16}O reaction. The reaction products were separated and detected by the a Q3D magnetic spectrometer, and a two-dimensional position-sensitive silicon detector recorded the position and energy information of the emitted particles. Figure 12 shows the typical focal-plane position spectrum of ^{7}Li at $\theta = 10°$ from the ^{12}C(^{11}B,^{7}Li)^{16}O$_{g.s.}$ reaction. The events in different reactions were clustered in different horizontal lines owing to having the same magnetic rigidity and different energies.

The angular distribution of the ^{11}B+^{12}C elastic scattering reaction was measured at the beginning and end of each angle to monitor the change in the target thickness and derive the optical potential of the entrance channel. We also measured the ^{7}Li+^{16}O elastic scattering reaction at an energy of 26 MeV to derive the optical potential of the exit channel.

Finite-range distorted-wave Born approximation (FRDWBA) calculations were performed to derive the ANCs of the ground, 6.917-MeV 2^+, and 7.117-MeV 1^- states using the FRESCO code [120]. The parameters required in the FRDWBA calculations were the optical potentials of the entrance channel (^{11}B + ^{12}C), exit channel (^{7}Li + ^{16}O), and core–core channel (^{7}Li + ^{12}C), and the binding potential parameters of ^{16}O and ^{11}B. The parameters of the entrance and exit channels were calculated using a single-folding model [121, 122]. Hartree–Fock calculations with the SkX interaction [123] were used to obtain the nucleon density distributions of ^{11}B, ^{12}C, and ^{16}O. The nucleon density distribution of ^{7}Li was taken

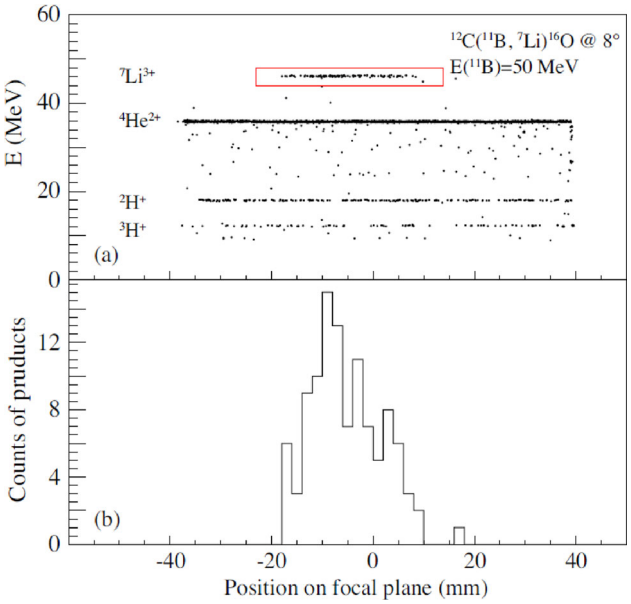

Fig. 12 Focal plane position spectrum of ^{7}Li at θ = 10° from the ^{12}C(^{11}B,^{7}Li)^{16}O$_{g.s.}$ reaction[117]

from an independent particle model [124]. These density distributions were folded using the systematic nucleon-nucleus potential of the JLMB model [125]. The depths of these single-folding potentials were adjusted by normalizing the parameters to provide an optimum reproduction of the experimental data with the optical model. The uncertainties in the normalized parameters of the single-folding potentials of the entrance and exit channels were evaluated based on a least-squares minimization procedure. To obtain the SF and ANC of the α-cluster in ^{16}O, the spectroscopic amplitudes of the α-cluster in the g.s. of ^{11}B were required. $S_{^{11}\mathrm{B},^{3}\mathrm{S}_0}$ and $S_{^{11}\mathrm{B},^{2}\mathrm{D}_2}$, taken from a former measurement of ^{7}Li(^{6}Li, d)^{11}B [126], are the single-particle wave functions describing the relative motion between an α-cluster and the

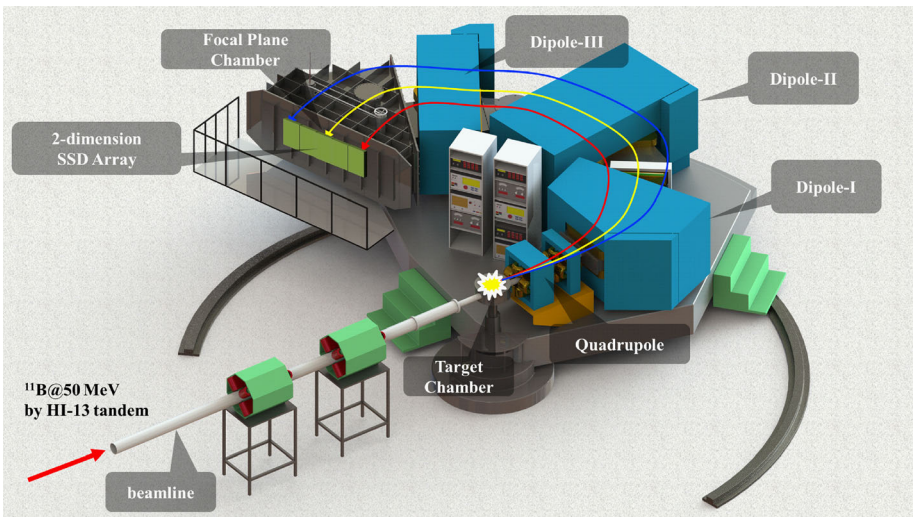

Fig. 11 (Color online) Setup used for the ^{12}C(^{11}B, ^{7}Li)^{16}O experiments

^{7}Li core in the ^{11}B g.s. for quantum numbers $NL_j = 3S_0$ and $2D_2$, respectively.

Next, we present the first determination of the g.s. ANC of ^{16}O using the ^{12}C(^{11}B,^{7}Li)^{16}O transfer reaction. With the new g.s. ANC values, we performed *R*-matrix calculations to illustrate the impact of external capture on the uncertainty of the ^{12}C(α, γ)^{16}O reaction. We obtained the astrophysical S_{E1} (300) and S_{E2} (300) factors of the g.s. transitions to be 55.3 $\pm$ 9.0 keV b and 46.2 $\pm$ 7.7 keV b, respectively. The GS S_{E2} (300) factor was obtained as 70 $\pm$ 7 keV b, resulting in an increase in the total *S*-factor from 140 to 162 keV b.

We also calculated the ^{12}C(^{11}B,^{7}Li)^{16}O reaction rates. Our reaction rate was approximately 20% larger than deBoer's value [3]. Following the calculation of Farmer et al. [53, 54], we calculated the BH masses. The calculated BH masses as a function of the initial He-core mass are shown in Fig. 13 [127–130]. The present reaction rate decreased the lower and upper edges of the BH mass gap by approximately 12% and 5%, respectively.

4.2 Indirect measurement using the surrogate ratio method

Both nuclear reactors on the Earth and massive stars in the Universe contain abundant unstable nuclei with half-lives of several days to millions of years combined in their fuels. Neutron radiative capture reactions of such radionuclides play an important role in energy generation and nucleosynthesis [131, 132]. To date, the cosmic origin of elements heavier than iron is believed to be slow and rapid neutron-capture processes, and many (n,γ) reactions of radionuclides are intensely involved in the relevant reaction networks. The competition between the β-decay and neutron capture of these unstable nuclei decides the nucleosynthesis path and changes the abundances of the follow-up nucleus. Furthermore, the abundances of the unstable nuclei's neutron-capture products are related to the neutron densities in massive stars, and the products of the unstable nuclei may be an effective probe to study the neutron density and related temperature inside. However, the (n,γ) cross sections are difficult to measure directly owing to the challenge in preparing the target materials of short-lived radionuclides. Therefore, several indirect methods have been proposed, and many experimental investigations have been conducted. The surrogate method (SM) [133, 134], which was first introduced in the 1970s for the extraction of neutron-induced fission cross sections, was recently used to determine (n,γ) reaction cross sections. Based on the Weisskopf–Ewing limit of Hauser–Feshbach theory [135], which assumes that the decay probability of a compound nucleus (CN) is independent of its spin parity, the method makes use of a surrogate reaction with an available beam and target to produce the same CN as the neutron-capture process. The cross section of the (n,γ) reaction is then indirectly determined by multiplying the calculated CN formation cross section by the measured γ decay probability.

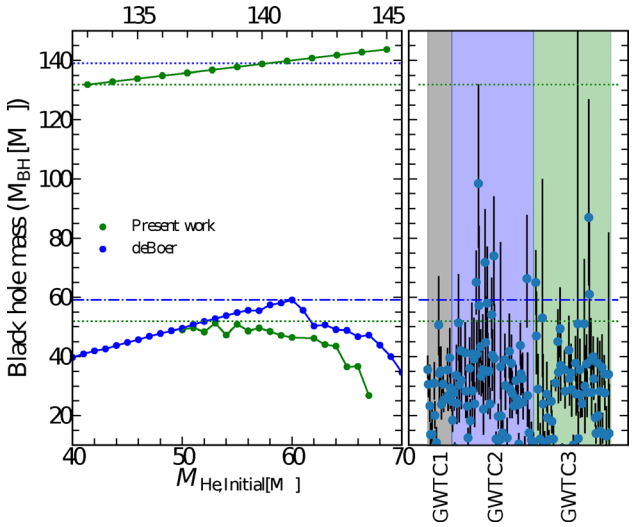

Fig. 13 (Color online) Black hole (BH) masses as a function of the initial helium-core mass with respect to the updated ^{12}C(^{11}B,^{7}Li)^{16}O reaction rate [127]. The blue dots connected by a line in the left panel represent the results obtained using the rates from [128, 129], and the green dots connected by a line represent the results obtained using the new CIAE rates. The boundaries of their BH mass gap are represented by the blue dashed-dotted lines and green dotted lines, respectively. The right panel shows the masses of the BH from the first, second, and third Gravitational-Wave Transient Catalogs (GWTC1, GWTC2, and GWTC3), which restrict the median estimated mass of the primary to $\geq 10M_{\odot}$, with 90% confidence intervals [130]

The SRM is a variation in the SM. In this method, two surrogate reactions are employed to obtain the relative γ-decay probability ratio. With an available A1(n,γ)B1 reaction cross section as the reference, the A2(n,γ)B2 reaction cross section can be obtained by multiplying the reference reaction cross section by the measured ratio:

$$\frac{\sigma_{\mathrm{A1(n,\gamma)B1}}(E_{\mathrm{n}})}{\sigma_{\mathrm{A2(n,\gamma)B2}}(E_{\mathrm{n}})} \approx C_{\mathrm{nor}} \frac{N_{\mathrm{B1^{*}}\gamma}(E_{\mathrm{n}})}{N_{\mathrm{B2^{*}}\gamma}(E_{\mathrm{n}})}, \quad (1)$$

C_{nor} is the normalization factor defined by experimental conditions, including the target thickness, beam current, and detector efficiency. $N_{\mathrm{B^{*}}\gamma}(E_{\mathrm{n}})$ is the number of CNs that decay into the g.s. by emitting γ-rays. Details can be found in [136]. The SRM has been successfully applied to determine the (n,f) cross sections [137–139], and a comprehensive review was recently published by Escher et al. [23]. In the case of (n,γ) reactions, theoretical studies [140, 141] indicate that the γ-decay probability is more sensitive to the spin-parity of CNs in the low-neutron-energy region. To apply the SRM to (n,γ) reactions, two-

neutron transfer reactions (^{18}O,^{16}O) were employed to verify the SRM to determine the (n,γ) reaction cross section in the neutron-rich nuclei region. In this benchmark experiment, the ^{91}Zr(n,γ)^{92}Zr and ^{93}Zr(n,γ)^{94}Zr reactions were chosen to check the SRM. In the measurements, the ^{90}Zr(^{18}O,^{16}O) and ^{92}Zr(^{18}O,^{16}O) reactions were used to produce the CNs ^{92}Zr* and ^{94}Zr*, instead of the (n,γ) reactions. The γ-rays emitted in the deexcitation of the CNs ^{92}Zr* and ^{94}Zr* were detected in coincidence with outgoing ^{16}O particles to obtain the ratio $N_{^{94}\mathrm{Zr}^*\gamma}(E_\mathrm{n})/N_{^{92}\mathrm{Zr}^*\gamma}(E_\mathrm{n})$. The indirectly determined ^{93}Zr(n,γ)^{94}Zr cross section with the SRM was then compared with the directly measured value [142].

The measurement was conducted at the tandem accelerator of the Japan Atomic Energy Agency (JAEA). An ^{18}O beam with an energy of 117 MeV was bombarded on an isotopically enriched zirconium target, which was constructed in the form of self-supporting metallic foil. Downstream of the target, a silicon $\Delta E - E$ telescope was used to identify the light ejectile particles. Two $LaBr_3$(Ce) detectors were used for γ-ray detection. A faraday cup was installed to collect the ^{18}O beam current for normalization purposes. After data analysis, the γ-decay probability ratios were obtained in a wide equivalent neutron energy range of 0-8 MeV with $N_{^{92}\mathrm{Zr}^*\gamma}(E_\mathrm{n})$ and $N_{^{94}\mathrm{Zr}^*\gamma}(E_\mathrm{n})$. The ^{93}Zr($n$,$\gamma$)^{94}Zr reaction cross sections were then determined relative to the cross sections of the ^{91}Zr(n,γ)^{92}Zr reaction together with the deduced γ-decay probability ratios, as shown in Fig. 14.

The deduced ^{93}Zr(n,γ)^{94}Zr reaction cross sections were found to be lower than the ENDF/B-VII.1 data at E_n = 1–3 MeV, whereas at $E_\mathrm{n} < 1$ MeV and $E_\mathrm{n} > 3$ MeV, the deduced cross sections agreed well with the directly measured and ENDF/B-VII.1 data. Although the absolute SM may suffer from the spin-parity sensitivity problem in the low-neutron-energy region, the data imply that the sensitivity of the γ-decay probability ratio to the CN spin-parity distribution is partially reduced in the SRM. Furthermore, the SRM data can be used to provide a restriction of the model parameters in theoretical calculation in the relatively high-neutron-energy region, which in turn provides a reasonable estimation of the (n,γ) cross sections in the low-energy region.

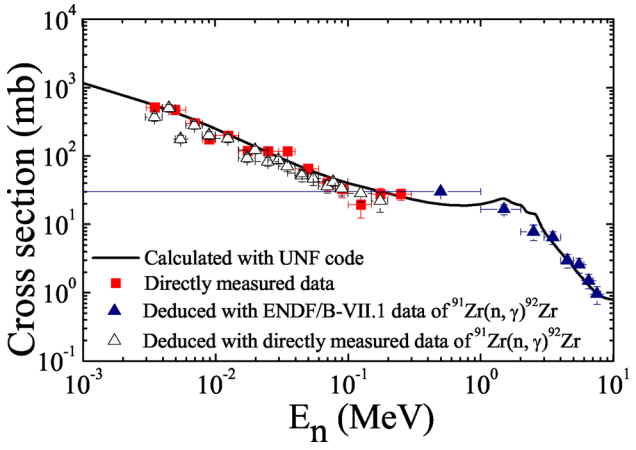

Fig. 14 (Color online) Cross section of ^{93}Zr(n,γ)^{94}Zr. The red squares are the directly measured data, the open triangles are data deduced by the γ-decay probability ratio and ^{91}Zr(n,γ)^{92}Zr cross sections, the blue triangles are data deduced by the γ-decay probability ratios and ^{91}Zr(n,γ)^{92}Zr ENDF/B-VII.1 cross section, and the solid curve is the results calculated using the UNF code after constraining the parameters via experimental data [142]

After validating the SRM in the determination of the (n,γ) cross section, the neutron-capture cross sections of the unstable nuclei ^{95}Zr and ^{59}Fe were measured indirectly.

Zirconium is a typical *s*-process element belonging to the first *s*-process peak and is mostly produced by the main component in AGB stars. Its isotopic abundances are sensitive to both neutron exposure and neutron density and thus critical to constrain the *s*-process in AGB stars [143]. The most neutron-rich stable Zr isotope, ^{96}Zr, is highly sensitive to neutron density during the *s*-process because its production depends on the activation of the branching point at ^{95}Zr (with a half-life of 64 d) for neutron densities above approximately 10^{10} cm^{-3}. However, although the neutron cross sections of stable Zr isotopes have been carefully studied, the cross section of the ^{95}Zr(n,γ)^{96}Zr reaction remains highly uncertain. Therefore, the SRM can be used to determine the ^{95}Zr(n,γ)^{96}Zr cross section indirectly. A measurement was conducted at the JAEA with a similar experimental setup, details of which can be found in [142]. In this measurement, the ^{94}Zr(^{18}O, ^{16}O)^{96}Zr* and ^{90}Zr(^{18}O, ^{16}O)^{92}Zr* reactions were used to form the CNs ^{96}Zr* and ^{92}Zr*, respectively. When $N_{^{92}\mathrm{Zr}^*}(E_\mathrm{ex})$ and $N_{^{96}\mathrm{Zr}^*}(E_\mathrm{ex})$ were obtained from experiments, the cross sections of ^{95}Zr(n,γ)^{96}Zr could be determined via the ^{91}Zr(n,γ)^{92}Zr cross sections and experimental ratios. The determined cross sections of ^{95}Zr(n,γ)^{96}Zr are shown in Fig. 15.

The radioactive isotope ^{60}Fe with a half-life of $\sim$2.6 million years has been of great interest to the nuclear astrophysics community for several decades. The presence of ^{60}Fe in the interstellar medium of our Galaxy was confirmed through the detection of 1173- and 1332-keV γ-rays from the decay of its daughter ^{60}Co ($t_{1/2}$ = 5.27 yr) by the RHESSI and INTEGRAL satellites. Because the half-life of ^{60}Fe is considerably shorter than the age of the Galaxy, the observations provide strong evidence of ongoing stellar nucleosynthesis. ^{60}Fe has also been observed in deep ocean ferromanganese crusts, nodules, sediments, snow from Antarctica [144–149], and even lunar regolith [150], which indicates the occurrence of

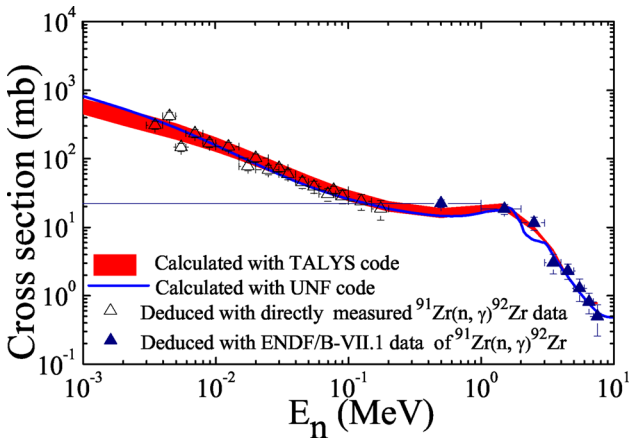

Fig. 15 (Color online) Cross section of ^{95}Zr(n,γ)^{96}Zr. The open triangles are deduced by multiplying our γ-decay probability ratio by the directly measured ^{91}Zr(n,γ)^{92}Zr cross section, and the blue triangles are deduced by multiplying our γ-decay probability ratios with the ENDF data for the ^{91}Zr(n,γ)^{92}Zr cross section. The blue curve is the theoretical calculation of the UNF code with parameters constrained by the experimental data in the high-energy region, and the red band is the uncertainties of the calculation results of the TALYS code with five sets of parameters constrained by the experimental data in the high-energy region [142]

more than one nearby supernova event within several 10^6 years.

To elucidate the production of ^{60}Fe in massive stars, a clear understanding of the ^{59}Fe(n,γ)^{60}Fe reaction is necessary. Based on the SRM, we measured the γ-decay probability ratios of the CNs ^{60}Fe* and ^{58}Fe*, which were populated by the two-neutron transfer reactions of ^{58}Fe(^{18}O,^{16}O) and ^{56}Fe(^{18}O,^{16}O). Subsequently, the ^{59}Fe(n,γ)^{60}Fe cross sections were determined using the measured ratios and directly measured ^{57}Fe(n,γ)^{58}Fe cross sections. The determined cross sections of ^{59}Fe(n,γ)^{60}Fe are shown in Fig. 16, and further details can be found in [151].

4.3 Indirect measurement of the ^{25}Mg(p,γ)^{26}Al reaction with the ANC method

^{25}Mg(p,γ)^{26}Al is the most important reaction during the Mg-Al cycle in the H-burning regions of stars. Its cross sections at stellar energies are essential to understanding the issues of radioactive ^{26}Al in the Galaxy and meteorites [98, 99]. The 57.7-keV resonance dominates the ^{25}Mg(p,γ)^{26}Al astrophysical reaction rates at relatively low temperatures; however, measuring its resonance strength directly can be challenging, and indirect measurement results deviate by a factor of approximately 2 [152–154].

A ^{25}Mg(^{7}Li,^{6}He)^{26}Al experiment was conducted using the Q3D magnetic spectrometer [119] with a 31.5-MeV ^{7}Li

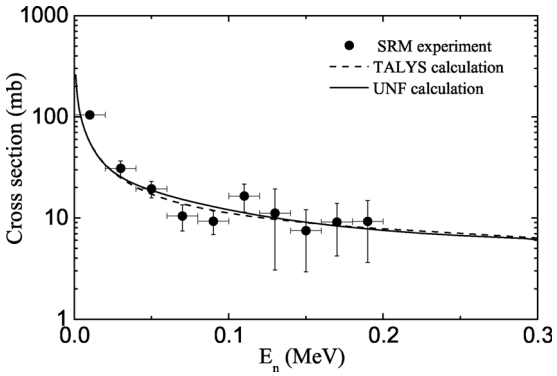

Fig. 16 Variation in the cross section of ^{59}Fe(n,γ)^{60}Fe as a function of equivalent neutron energy. The circles are obtained by multiplying the experimental γ-decay probability ratio by the directly measured ^{57}Fe(n,γ)^{58}Fe cross section. The dashed and solid curves represent the calculated results according to UNF and TALYS codes, respectively, with their parameters constrained by the γ-decay probability ratios of CN ^{60}Fe* and ^{58}Fe* in the high-energy region [151]

beam from the CIAE HI-13 tandem accelerator. The angular distribution of the ^{25}Mg(^{7}Li,^{6}He)^{26}Al$^{6.364}$ reaction was measured as the first objective in this experiment. Moreover, the transfer reactions leading to the g.s. and first ten excited states were measured deduce the direct capture component of ^{25}Mg(p,γ)^{26}Al and verify the SF proportions for different angular momentum components calculated from the shell model (Fig. 17). To extract the optical potential of the entrance channel, the angular distribution of ^{7}Li elastic scattering on ^{25}Mg was also measured [155].

The proton SFs of ^{26}Al were analyzed with the shell model code NUSHELL using usdbpn Hamiltonian [156] in the sdpn model space, and the calculated ratios of the $2s_{1/2}$, $1d_{3/2}$, and $1d_{5/2}$ orbits were adopted in the DWBA analysis. The angular distributions of the ^{25}Mg(^{7}Li,^{6}He)^{26}Al transfer reaction leading to 12 states in ^{26}Al were well reproduced with J^π from 0^+ to 5^+ and the varied proportion of $2s_{1/2}$, $1d_{3/2}$, and $1d_{5/2}$ components. Subsequently, the proton SFs of the 6.364-MeV state in ^{26}Al were derived to be 0.082±0.012, 0.162±0.024, and 0.028±0.004 for the $2s_{1/2}$, $1d_{3/2}$, and $1d_{5/2}$ orbits, respectively. The present SFs are in agreement with the reanalysis results of three (^{3}He,d) reactions [152–154].

Based on these SFs, the proton width and resonant strength of the 57.7-keV resonance in the ^{25}Mg(^{7}Li,^{6}He)^{26}Al reaction were deduced, and the astrophysical ^{25}Mg(^{7}Li,^{6}He)^{26}Al reaction rates were updated. The present results provide independent examinations of the ^{26}Al$^{6.364}$ proton SFs and 57.7-keV resonance strength. The ^{25}Mg(^{7}Li,^{6}He)^{26}Al reaction rates increased by approximately 5% at T 0.1 GK, and the uncertainties were significantly reduced.

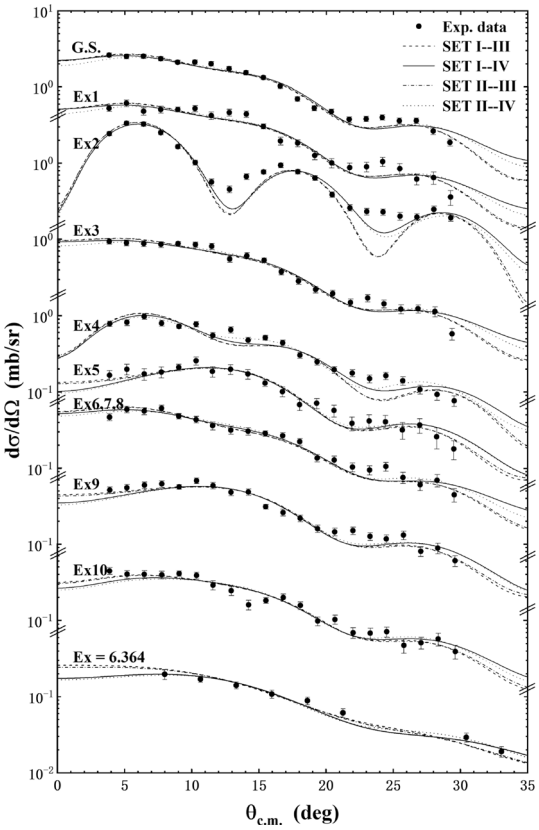

Fig. 17 Measured angular distributions of the ^{25}Mg(^{7}Li,^{6}He)^{26}Al transfer reactions together with the DWBA calculations [155]

4.4 Novel thick-target inverse kinematics method for the astrophysical ^{12}C+^{12}C fusion reaction

^{12}C+^{12}C fusion reactions play a crucial role in stellar evolution and explosive phenomena within the Universe [55, 157, 158], particularly during the final stage of massive star evolution, Type Ia supernovae (SNe Ia) events [159], and superbursts [160, 161]. The temperatures and densities [162] required for the ignition of carbon burning in massive stars and the superburst ignition depth in accreting neutron stars strongly depend on the ^{12}C+^{12}C reaction rate, which still remains elusive, to reconcile observations with theoretical models [163]. The Gamow peak of these reactions is 1.5 MeV at a temperature of 0.5 GK, which is far below the Coulomb barrier height of the ^{12}C+^{12}C system, at around 7.5 MeV. Thus, the cross section decreases rapidly in the energy region of interest and is yet to be reported from direct measurements below 2.1 MeV [164–172].

A series of direct measurement data suggest the existence of sub-barrier resonances in the ^{12}C+^{12}C fusion reaction [168–170], leading to significantly enhanced reaction rates compared with the standard non-resonance rate given by Caughlan et al. [173, 174]. Owing to the presence of potential resonances in the unmeasured energy ranges, it is extremely difficult to provide an extrapolation to the lower energies, including the Gamow energy region for the ^{12}C+^{12}C fusion reaction. Therefore, determining the resonance parameters of proton and α decaying channels is extremely important in the Gamow energy region.

A thick-target inverse kinematics (TTIK) measurement was conducted for ^{23}Na+p [114, 175] at the CIAE HI-13 tandem accelerator. The experiment setup is shown in Fig. 18. A ^{23}Na beam with an energy of 110 MeV was delivered and directed onto a self-supporting $(CH_2)_n$ target. A thick carbon target was used to measure the background. For the measurement of the excitation functions, the particles emitted in the ^{23}Na+p and ^{20}Ne+α exit channels were detected with a silicon telescope system at 0° along the beamline. The silicon telescope system consisted of a 70-μm double-sided silicon strip detector (DSSD), 1.5-mm multi-guard silicon quadrant (MSQ), and 1-mm MSQ. Six three-inch $LaBr_3$ detectors were uniformly arranged around the target chamber to measure the characteristic γ rays from the residual nuclei ^{23}Na and ^{20}Ne.

In the relevant energy range, the exit channels of compound ^{24}Mg consisted of p_0, p_1, α_0, and α_1. For the residual nuclei ^{23}Na and ^{20}Ne, the full-energy peak efficiencies at characteristic energies of 440 keV and 1634 keV were 28.2 % and 12.6 %, respectively.

The energy spectrum of charged particles obtained by silicon detectors contains a series of excitation function effects. Through the data analysis process, including γ-charged particle coincidence, two-body reaction kinematics reconstruction, and carbon background deduction, the excitation functions of the CN ^{24}Mg populated by the ^{23}Na+p entrance channel were obtained, as shown in Fig. 19. *R*-matrix analysis was performed to extract a series of exit channel resonance parameters. Nearly fifty ^{24}Mg resonances were introduced to reproduce the excitation functions, including those most relevant to the ^{12}C+^{12}C fusion reaction. The branching ratios and astrophysical *S*-

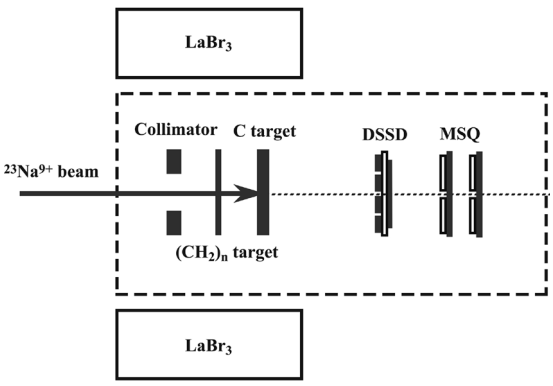

Fig. 18 Setup of the ^{23}Na+p thick-target experiment [114]

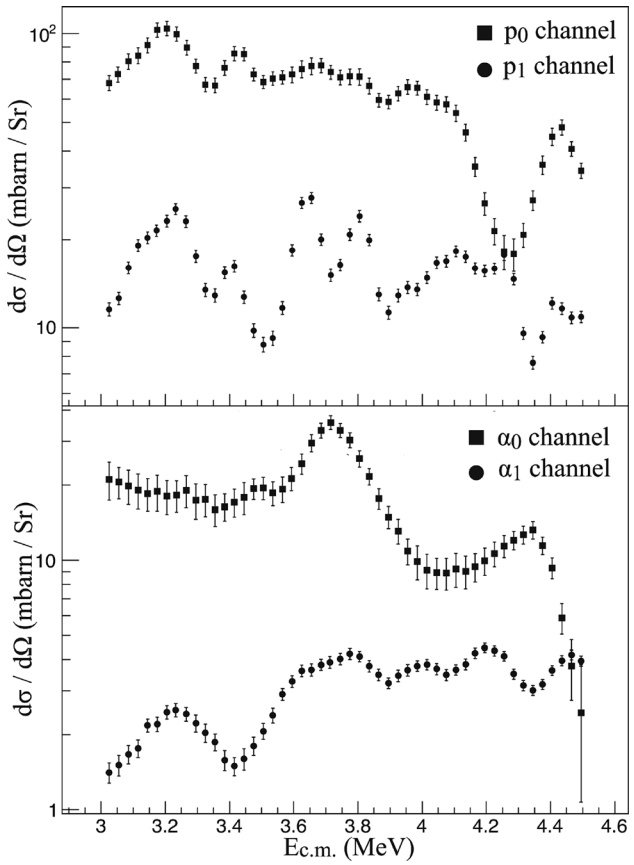

Fig. 19 Excitation functions for the proton and α exit channels. p_0, p_1, and α_0, α_1 represent ^{1}H(^{23}Na, p_0)^{23}Na, ^{1}H(^{23}Na, p_1)^{23}Na$^{*}_{440}$, and ^{1}H(^{23}Na, α_0)^{20}Ne, ^{1}H(^{23}Na, α_1)^{20}Ne$^{*}_{1634}$, respectively. The error bars primarily account for accidental coincidence errors, statistical uncertainties, carbon background, and $p_1(\alpha_1)$ errors in the $p_0(\alpha_0)$ calculation. See [114] for details

factors of different decay channels were evaluated with the theoretically calculated reduced width of the ^{12}C+^{12}C entrance channel. Our analysis revealed that the sharp increase in the astrophysical *S*-factor reported by Tumino et al. disappeared, which is consistent with the results from antisymmetrized molecular dynamics calculations [176].

5 Measurement of the D(*d*, *n*)^{3}He and ^{7}Li(*d*, *n*)^{8}Be reactions in laser-induced full plasma

In recent years, with the rapid development of laser technology, lasers have become a new tool for studying nuclear science [177, 178], following accelerators and reactors. Meanwhile, a new interdisciplinary field known as laser nuclear physics has also emerged. Research on nuclear reactions in extreme plasma environments based on strong laser devices has a significant demand in cutting-edge fields and applied science. This is because in the fields of nuclear physics and high-energy-density physics research, strong lasers are an important means of generating a star-like or high-energy-density environment in the laboratory. They are ideal for studying the nuclear reaction mechanism in high-temperature and high-density plasma environments [179, 180]. Therefore, laser technology is of great significance for better understanding some long-existing puzzles related to nucleosynthesis, such as the puzzles of the Big Bang lithium abundance and ^{26}Al abundance [181], as well as understanding the impact of extreme plasma environments on nuclear parameters.

5.1 Direct calibration of neutron detectors for laser-driven nuclear reaction experiments

In nuclear physics experiments with laser-induced plasma, quantitatively measuring the reaction products is highly challenging because of the interference of electromagnetic pulses (EMP) induced by high-intensity lasers. Fast scintillation detectors with time-of-flight (TOF) detection are widely chosen for fast neutrons [182–184]. The calibration of neutron detectors is crucial for measuring the yield of neutron products. However, energy calibration methods for detection systems aimed at laser-induced plasma environments have not yet been systematically demonstrated.

In a previous study [185], we developed a direct calibration method with a gated fission neutron source ^{252}Cf to solve this problem. This study demonstrated that the gated fission neutron source approach, with an unique "window" function, exhibited the highest background-γ-rejection. It also improved upon the confidence level of the final results of both liquid and plastic scintillators obtained from the Compton edge and neutron beam methods.

The gated fission neutron source approach is a direct experimental calibration method. The experimental setup of the gated calibration with a fission neutron source can be found in [185], where a ^{252}Cf source with a neutron activity of 10^{2} Bq was used. Its spontaneous fission neutron spectrum was determined as the standard neutron spectrum by International Atomic Energy Agency (IAEA) [186], which is typically used to calibrate the efficiency of neutron detectors [187, 188]. For each fission, on average, 3.6 neutrons are emitted from ^{252}Cf, and around 9.3 gammas are simultaneously emitted from the rapid decay of the fission fragments [189]. Thus, one can construct the TOF between the neutrons and prompt gamma. Therefore, both the companion gamma signals (recorded by the plastic EJ200 scintillator) and neutron signals (recorded by the scintillation detector to be calibrated) were used as the triggers to open the AND logic gate to start the recording process of the digitizer DT5730SB. To analyze the AND gate, the interval between the prompt gamma and one

neutron signal was adjusted appropriately according to the neutron energy to reduce background interference. For the calibration of 2.45-MeV neutrons, the time interval was set as 120 ns, whereas the recording period was set as 600 ns. After the AND gate was opened, the waveforms of the neutron signals from the to-be-calibrated neutron detectors were recorded by the digitizer, as shown in Fig. 20.

As shown in Fig. 20, the background interference in the calibration experiment was significantly reduced because the gamma signals recorded by the EJ200 and the neutron signals were simultaneously used to determine whether to open the AND gate to start recording the signals. Furthermore, because the scintillator has different responses to a neutron or a gamma photon, they could be checked by analyzing the waveforms recorded by DT5730SB. Moreover, we distinguished the neutron signal from spurious gamma backgrounds with both the PSD and TOF functions simultaneously; hence, the background could be further reduced by using the pulse shape discrimination [190, 191] and TOF methods. Thus, the purity of neutron signals was significantly improved.

For comparison, we used two other popular methods to calibrate the neutron detectors. First, a direct calibration method was performed with the 2.45-MeV neutrons produced from the D(d,n)^{3}He reaction using the Cockcroft–Walton accelerator at the CIAE [192]. Second, an indirect calibration method commonly used with a Compton edge [193–195] was conducted. The comparison results for the three methods are shown in Table 4.

In conclusion, the gated fission neutron source method can directly produce the experimental calibration results of neutron yields from laser-driven nuclear reactions. It exhibits a higher background-γ-rejection rate, which improves the confidence level of the final results. Furthermore, with a more active ^{252}Cf fission source and optimized setup (longer distance, narrower gating, etc.), the calibration time may be shortened, and a more extensive energy range of neutrons and a smaller uncertainty can be achieved. Consequently, neutron yields from nuclear reactions in laser-induced plasma may be obtained more precisely. This method can provide an effective and straightforward calibration system for neutron detectors for future laser-driven nuclear fusions and laser-induced neutron sources.

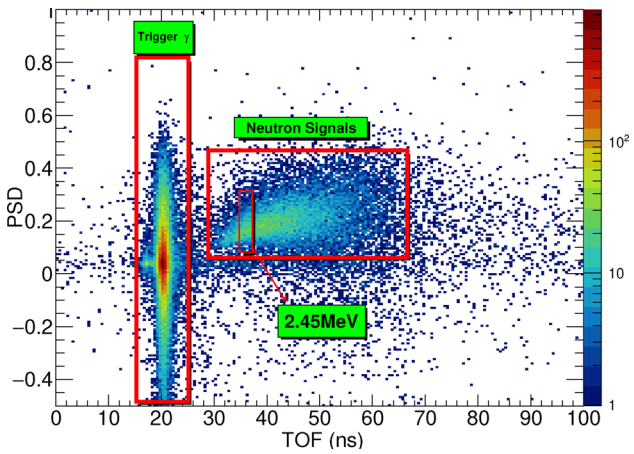

Fig. 20 (Color online) Two-dimensional spectrum of the PSD vs. TOF for neutron signal calibration [185]

5.2 Deuterium–deuterium fusion in nanowire plasma driven by a nanosecond high-energy laser

It is well known that in nuclear astrophysics, especially in the Gamow window, the energies of the ions of interest range from a few keV to hundreds of keV. Therefore, the interaction of nanosecond (ns) lasers with solid targets is well suited to generating extreme plasma environments in the above energy range. A previous study [196] found that, in nanowire form, nanostructures on the surface of the target could absorb laser energy with high efficiency. The nanowire target can generate an extreme plasma environment an order of magnitude higher in temperature and density than a planar target, and theoretical calculations indicate that the neutron yield is expected to be improved when a ns laser interacts with nanowire targets. However, the effect of the interaction between kJ-level ns lasers and nanowire targets on energy absorption and neutron yield is still unclear. In this study, based on the collision of two plasma streams, we first conducted an experimental study on kJ-level ns laser irradiation of a CD_2 nanowire target using the colliding plasmas method [197, 198] and evaluated the energy conversion efficiency between them by measuring the yield of nuclear reaction products.

The experiment [199] was performed at the ShenGuang II laser facility of the National Laboratory on High Power Lasers and Physics in Shanghai, China. Figure 21 shows a schematic diagram of the experimental setup with the target layer changed from LiD to CD_2 [200–202]. There were eight laser beams aimed at the center of the target chamber, and each beam could deliver an energy of approximately 250 J with a pulse width of 1 ns at a wavelength of 351 nm (3ω). A dual target was located at the center of the chamber. Both of the targets had 2.0 mm $\times$ 2.0 mm sized copper bases, which were coated with $200-500$ μm-thick deuterated hydrocarbon $(CD_{1.96}H_{0.04})_n$ layers. The opposing layers on the target were separated by 4 mm. The ns lasers were arranged as two sets ($4+4$), and each set had four lasers focusing on one side of the dual target. The diameter of the focal spots was approximately 150 μm, and the corresponding intensity was approximately 6×10^{15} W/cm^2. A TOF detection system was used with

Table 4 Comparison of the results from three calibration methods for different detectors [185]

Scintillator	Voltage	Neutron beam		Compton edge		Gated fission	
	(V)	Area[a]	σ[b]	Area	σ	Area	σ(%)
Liquid EJ301	−1600	0.88	350%	1.08	64%	0.93	46
Plastic BC420	−1300	–[c]		0.58	76%	0.65	50

[a] The unit of Area (average area) of a single neutron peak is ns·V,

[b] σ represents the relative uncertainty of the average results for a single neutron calibration,

[c] Plastic scintillator BC-420 does not have a PSD function and cannot derive neutron signals from gamma.

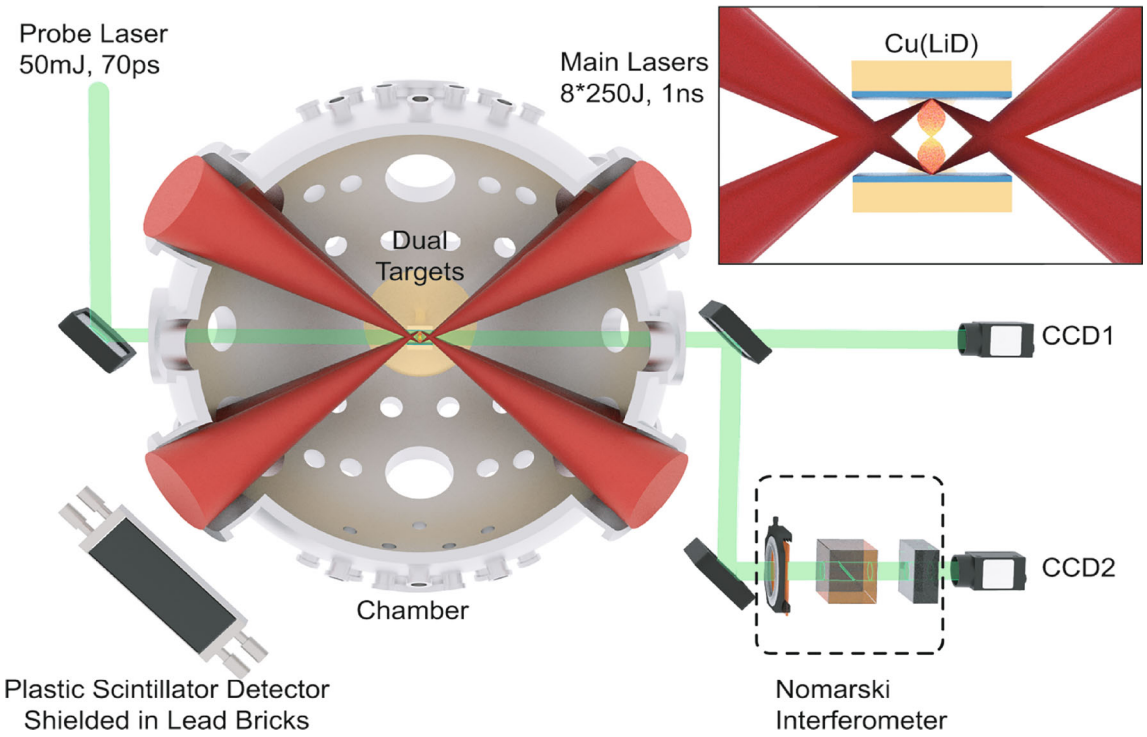

Fig. 21 (Color online) Schematic layout of the experimental setup. The materials of the main targets are lithium deuteride (LiD) with density $\rho_{\mathrm{LiD}} = 0.906\ \mathrm{g/cm^3}$ (see the enlarged illustration in the upper right corner). The counter-streaming plasmas are produced from the main targets via ablation with 4 laser beamlines. A lead-shielded plastic scintillator detector is used to record the neutron products. The interference images are taken by a Nomarski interferometer [204]

scintillation detectors and oscilloscopes to record the neutrons arriving at the detectors simultaneously and avoid the strong EMP impact on shooting time. The interaction between the counter-streaming plasma flows was measured with optical diagnostics, including Nomarski interferometry and shadow graphics, using a 9th probe laser with a duration of 70 ps and wavelength of 526 nm. The probe laser was passed through the plasma interaction zone generated by the main laser beams to achieve interference images. Meanwhile, snapshots of the plasma at different times were taken by changing the delay time between the probe and main lasers. Using the Abel inversion approach [203] for the interference data, the plasma density distribution was obtained.

The developed numerical calculation results indicated that as $E_{\mathrm{c.m.}}$ increased, the cross section increased, whereas the number of ions (N) increased and then decreased. Thus, as shown by the solid blue line in Fig. 22, the majority of the neutron yields originated from the $E_{\mathrm{c.m.}}$ energy range 10–30 keV. The neutron data from the EJ301 and BC420 detectors were calibrated using the gated fission neutron source ^{252}Cf method [185]. The neutron yields for various target specifications are displayed in Fig. 23 at the same order of 10^6 per shot. The systematic uncertainty was 47% for EJ301 and 51% for BC420.

The results indicate that the nanowire target could not significantly enhance the energy absorption of the ns laser, even with high energy, compared with the results of the planar target. This conclusion was supported by the

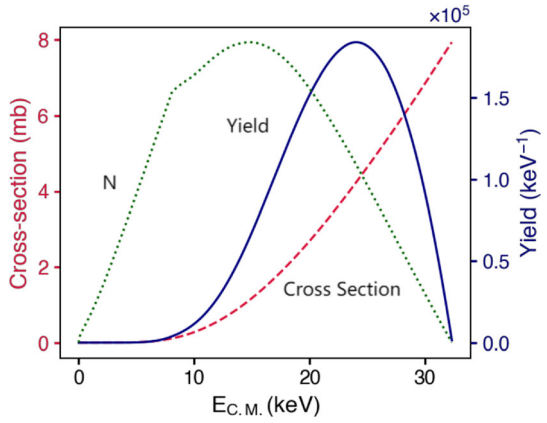

Fig. 22 Neutron yield contributed by deuterium ions with different $E_{c.m.}$ energies. Three data lines are shown in this chart: the number of the ions from the experimental diagnostic (dotted green line), D(d,n)^{3}He cross section (dashed red line), and calculated neutron yield (solid blue line) [199]

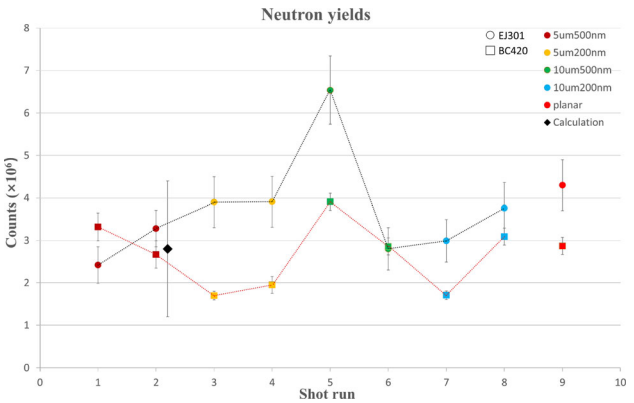

Fig. 23 (Color online) Neutron yields with statistical uncertainties from EJ301 and BC420 detection and different target parameters. The circles represent the results of EJ301 detection and the squares represent those of BC420. The black diamond represents the results of the numerical calculation with the optical diagnostics approach for the 2nd shot run. Different colors correspond to different target parameters [199]

experimental results, numerical calculation, and magneto-hydrodynamic simulation. Moreover, this study provides a useful experimental method for investigating nuclear reactions in a plasma environment with an energy region of interest of tens of keV in nuclear astrophysics.

5.3 Measurement of the ^{7}Li(d,n)^{8}Be astrophysical S-factor in laser-induced full plasma

Plasma is known as the fourth state in the universe and is composed of many ions, electrons, and other particles. In the process of laser-driven jet collision interactions, there are various instabilities, such as two-stream instability and Weibel instability, which may generate electromagnetic fields. In addition, there are also uncertainties in the energy and focal spot of each laser shot, which pose significant challenges in measuring the nuclear reaction during the experimental process. Using the collision method of two plasma jets, experimental research on the fusion reaction of ^{7}Li(d,n)^{8}Be in a plasma environment was conducted at the Shenguang-II laser facility, the National Laboratory on High Power Lasers and Physics, Shanghai, China. The experimental setup is schematically shown in Fig. 21. We established the theoretical model and numerical simulation method for studying the plasma collision process of the deuterium–lithium fusion reaction. We proposed an innovative method, namely, the Self-Calibration Method for Nuclear Reactions in Plasma (SCM-NRP), to eliminate the influence of plasma and laser parameter instability on experimental measurements. For the first time, we measured the astrophysical S-factor in plasma and obtained $S = (24 \pm 8)$ MeV · barn in the Gamow window around 173 keV, as shown in Fig. 24 [204]. We experimentally demonstrated that the plasma effect may not have a significant impact on the ^{7}Li consuming reaction related to the Big Bang lithium abundance puzzle near 173 keV. This study provides theoretical and experimental methods and data support for the development and application of research related to laser plasma and laser nuclear physics in the fields of fundamental nuclear physics and high-energy-density physics, promoting the development and cross integration of disciplines.

6 Advances in the theoretical study of supernova nucleosynthesis

Supernova explosions are one of the most spectacular astronomical events and the most important heavy-element synthesis factories in the Universe. The study of

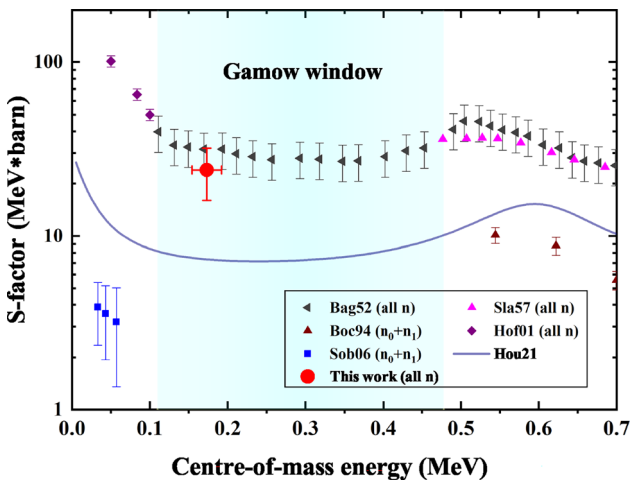

Fig. 24 (Color online) Comparison of the ^{7}Li(d,n)^{8}Be reaction astrophysical S-factors in full plasma (our study) and non-plasma environments (all other studies) [204]

nucleosynthesis in supernovae has significant implications for understanding the formation of the solar system, the chemical evolution of the Milky Way, and the evolution of the Universe.

6.1 Effect of metallicity on SNe Ia luminosity

Normal SNe Ia can serve as a cosmological standard candle to measure galactic distances, which can reveal cosmic motion and compositions when combined with cosmological models [205–207]. In fact, the light of an SNe Ia explosion originates from the decay of synthesized radioisotopes, and the peak luminosity is dominated by the amount of ^{56}Ni formed during the nucleosynthesis [208]. However, the ^{56}Ni yield is closely related to the initial metallicity of the SNe Ia progenitor ($Z_{\rm pro}$) [209, 210]. It is well known that main-sequence stars inherit the metal elements produced by previous stars from the ambient interstellar medium during their formation. Therefore, the initial metallicity of the SNe Ia progenitor should increase with the accumulation of heavy elements in the Universe, which would have an important effect on the synthesis of ^{56}Ni. A varying "standard candle" may then lead to misconceptions about the origin and evolution of the Universe.

Now, it is widely accepted that SNe Ia are produced by the thermonuclear explosion of a carbon-oxygen (CO) white dwarf in a binary system, whereas our understanding of the progenitor system, accretion rate, and explosion mechanism is still unclear [211–214]. Both near-Chandrasekhar mass (near-$M_{\rm ch}$) and sub-Chandrasekhar mass (sub-$M_{\rm ch}$) models are promising progenitor scenarios for SNe Ia. By analyzing the 1D, 2D, and 3D simulation results, we found that the ^{56}Ni yield depends linearly on $Z_{\rm pro}$,

$$M(^{56}\mathrm{Ni}) \propto 1 - b(Z_{\rm pro}/Z_{\odot}), \tag{2}$$

where $Z_{\odot}$ denotes the solar metallicity, and the slope b is approximately 0.050 and 0.078 for the sub-$M_{\rm ch}$ and near-$M_{\rm ch}$ models, respectively [215]. This suggests that the peak luminosity of the near-$M_{\rm ch}$ SNe Ia is more influenced by the initial metallicity of the progenitor than that of sub-$M_{\rm ch}$ SNe Ia.

It is difficult to measure the initial metallicity of SNe Ia progenitors either from the supernova remnants or their environments [216–220]. However, studies on cosmic mean metallicity (CMM) provide a possibility of estimating $Z_{\rm pro}$. Because the initial metal elements of the progenitors are inherited from their ambient interstellar medium, it is reasonable to consider that $Z_{\rm pro}$ roughly follows the CMM evolution. Many studies on CMM evolution have shown or implied that $\log_{10}(Z_{\rm CMM}/Z_{\odot})$ is approximately linear with redshift, at least in the range of $z<5$ [221–224].

$$\log_{10}(Z_{\rm CMM}/Z_{\odot}) = -az + a_0, \tag{3}$$

where a indicates the evolution rates of the CMM, which are approximately 0.22 and 0.15 according to the quasar absorption-line systems (QASs) and cosmic star formation rates (CSFRs). The QASs suggest a faster evolution rate of the CMM than the CSFRs.

After combining the two relationships, it is clear that the yield of the synthesized ^{56}Ni decreases with the cosmological chemical evolution, which indicates that the previous SNe Ia is brighter than the present when at the same distance. The relationship between distance modulus μ and luminosity distance $d_{\rm L}$ is corrected to

$$\mu = 5\log\left[d_{\rm L}\left(\frac{1-b\times 10^{az}}{1-b}\right)^{-\frac{1}{2}}\right] - 5, \tag{4}$$

where the solar metallicity is taken as the current CMM, that is, $a_0 = 0$. The luminosity distance can be further expressed as a function of redshift z and the current proportion of dark energy Ω_Λ based on the Λ cold dark matter (ΛCDM) model,

$$d_{\rm L} = \frac{1+z}{H_0}\int_0^z \left[(1-\Omega_\Lambda)(1+z')^3 + \Omega_\Lambda\right]^{-\frac{1}{2}} \mathrm{d}z', \tag{5}$$

where H_0 is the Hubble constant. Subsequently, Ω_Λ can be deduced using the measurements of the distance modulus μ and redshift z of the SNe Ia. The cosmic age can also be estimated using the following equation:

$$t_0 = \frac{2}{3H_0\sqrt{\Omega_\Lambda}}\ln\left(\frac{1+\sqrt{\Omega_\Lambda}}{\sqrt{1-\Omega_\Lambda}}\right). \tag{6}$$

Finally, the corrected dark energy proportions would be higher than the *Planck* results, and the Universe would be 0.2−0.4 billion years older than the previously estimated value (shown in Fig. 25) [215]. By studying the effect of metallicity on the SNe Ia luminosity, a more accurate distance scale can be obtained. The accurate measurement of intergalactic distances may clarify several major puzzles in current cosmology, including the Hubble tension, formation of the cosmic structures, and evolution of dark energy [225].

6.2 Neutrino nucleosynthesis in core-collapse supernovae

Massive stars typically undergo H, He, C, Ne, O, and Si burning and end up with iron-peak elements. When the mass of the iron core exceeds the effective Chandrasekhar mass, the core starts to collapse and a neutron star or a BH is formed. The gravitational binding energy of the proto-

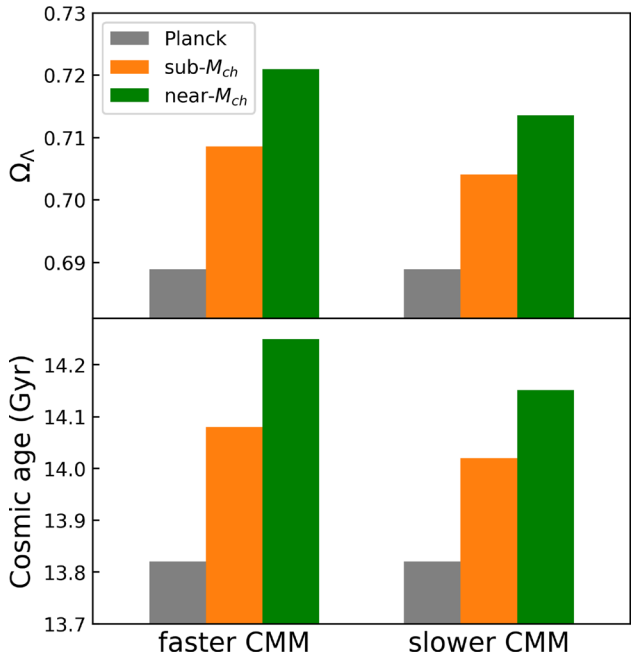

Fig. 25 (Color online) Dark energy proportions (Ω_Λ) and cosmic ages predicted using *Planck* measurements (gray columns), the sub-$M_{\rm ch}$ model (orange columns), and the near-$M_{\rm ch}$ model (green columns) with faster and slower CMM evolutions [215]

neutron star, $E_{\rm total}\sim 3\times10^{53}$ erg, is removed by a powerful stream of neutrinos during the cooling stage, which may have important implications for nucleosynthesis.

The total energy is approximately equally distributed among all six neutrino species, $\nu_e, \overline{\nu}_e, \nu_\mu, \overline{\nu}_\mu, \nu_\tau$, and $\overline{\nu}_\tau$, and the neutrino emission shows an exponentially decreasing luminosity $L = L_0 e^{-t/\tau_\nu}$ with the characteristic time $\tau_\nu = 3$ s [226]. Assume that the initial radius of the shell in which the seed nucleus resides is r_0, and the average shock velocity interior to r_0 is $v_{\rm sh}$. Before the arrival of the shock wave, the state of the shell remains almost unchanged. The radius is a constant, $r(t<t_0) = r_0$, and the temperature is approximately equal to the temperature of hydrostatic burning. When the shock wave arrives, the temperature increases instantaneously to a peak value [226],

$$T_{\rm peak} = 2.4\left(\frac{E_{\rm expl}}{10^{51}\ {\rm erg}}\right)^{1/4}\left(\frac{r_0}{10^9\ {\rm cm}}\right)^{-3/4}\ {\rm GK}, \tag{7}$$

where $E_{\rm expl}\sim 1.2\times10^{51}$ ergs is the total kinetic energy of the shock. Then, the overpressure drives rapid expansion. The expansion of the shocked mass element is approximately adiabatic, and its temperature decreases exponentially with the hydrodynamic time scale $\tau_{\rm HD}$ [226],

$$T(t) = T_{\rm peak} e^{-(t-t_0)/3\tau_{\rm HD}}, \tag{8}$$

where $\tau_{\rm HD}\approx 446\rho^{-1/2}$ s, and ρ in units of g/cm^3 is the mean density within the radius r_0 (that is, $r<r_0$). The shocked material in the outer layer of the star is assumed to be moving at a typical constant speed $v_{\rm p}$ in the expansion phase. Therefore, the neutrino flux is [226]

$$\phi_\nu(t) = \begin{cases} \phi_{\nu,0} e^{-t/\tau_\nu}, & t<t_0, \\ \phi_{\nu,0} e^{-t/\tau_\nu}\left[1+(t-t_0)/\tau_{\rm p}\right]^{-2}, & t>t_0, \end{cases} \tag{9}$$

where

$$\phi_{\nu,0} = \frac{E_{\rm total}\tau_\nu^{-1}}{4\pi r_0^2 n_{\rm f}\langle E_\nu(T_\nu)\rangle}, \tag{10}$$

where $n_{\rm f}=6$ is the number of neutrino species and $\langle E_\nu(T_\nu)\rangle$ is the average energy of the neutrinos.

For the $\nu_{\rm e}$-process $(Z,A)+\nu_{\rm e}\rightarrow(Z+1,A)+e^-$, the abundance ratio of the daughter nucleus to parent nucleus satisfies the differential equation

$$\dot{\mathcal{R}}(T_\nu,t) = \phi_\nu(t)\langle\sigma_\nu(T_\nu)\rangle - [\lambda_\beta(T)+\lambda_\gamma(T)]\mathcal{R}(T_\nu,t), \tag{11}$$

where the first term on the right side denotes the production rate of the daughter nucleus via the $\nu_{\rm e}$-process, whereas the second term denotes the destruction rate via $\beta^\pm$ decay and photodisintegration. The expression for the $\nu_{\rm e}$-nucleus cross section for a specific nucleon state X has the following form [227]:

$$\sigma_X(E_\nu) = \frac{G_{\rm F}^2\cos^2\theta_{\rm C}}{\pi} g_{\rm V/A}^2 B(F/GT) p_{\rm e} E_{\rm e} F(Z_{\rm f}, E_{\rm e}), \tag{12}$$

where $G_{\rm F}$ is the Fermi constant, $\theta_{\rm C}$ is the Cabibbo angle, $g_{\rm V}$, and $g_{\rm A}$ are the vector and axial-vector interaction constants, respectively, $B(F/GT)$ is the square of the Fermi/Gamov–Teller nuclear matrix element for transition to a certain state of the final nucleus, divided by $(2J_i+1)$, E_ν is the energy of the incoming neutrino, and $E_{\rm e}$ and $p_{\rm e}$ are the energy and momentum of the outgoing electron, respectively. The Fermi function $F(Z_{\rm f}, E_{\rm e})$ contains a Coulomb correction of the lepton and the daughter nucleus in the final state. The quantity entered into the calculations is the total cross section [228],

$$\langle\sigma_\nu(T_\nu)\rangle = \sum_X \int_{E_{\rm th}}^{\infty} \Phi(E_\nu,T_\nu)\sigma_X(E_\nu){\rm d}E_\nu, \tag{13}$$

where $E_{\rm th}$ is the threshold energy of the reaction. $\Phi(E_\nu,T_\nu)$ is the neutrino spectrum, which is assumed to follow a Fermi–Dirac distribution with a vanishing chemical potential [226, 228, 229].

We considered the effects of neutrino temperature and shock velocity at different shell radii, and the maximum yields of ^{26}Al and ^{74}Se were found at $r_0 = 11000$ and 8000 km, respectively (shown in Figs. 26 and 27, respectively) [230, 231]. After considering the Galactic mass distribution, we estimated that the total mass of ^{26}Al produced via the ν_e-process was $0.16 \pm 0.08\ M_\odot$ by taking solar metallicity as representative (marked as $Z_\odot$) and $0.23 \pm 0.13\ M_\odot$ by using the Galactic metallicity distribution (marked as $Z(r_G)$) (shown in Fig. 28) [230]. The ν_e-process could contribute 10% of the ^{26}Al mass estimated from the γ-ray observation [232]. These results are consistent with those of previous studies, which suggested that approximately 0.2 $M_\odot$ of ^{26}Al is contributed by the neutrino process [229, 232]. Furthermore, it is worth emphasizing that this semi-analytic approach allows us to deviate from the extremely time-consuming numerical simulations and carefully study the influences of several important factors, such as shell radius, shock velocity, neutrino spectrum, Galactic mass, and metallicity distribution. We conclude that the biggest uncertainty originates from the neutrino spectrum, while the second-most important uncertainties arise from the initial mass function of stars and the core-collapse supernovae formation rate [230]. Therefore, these studies facilitate an intuitive understanding of the buried implicit assumptions in previous studies.

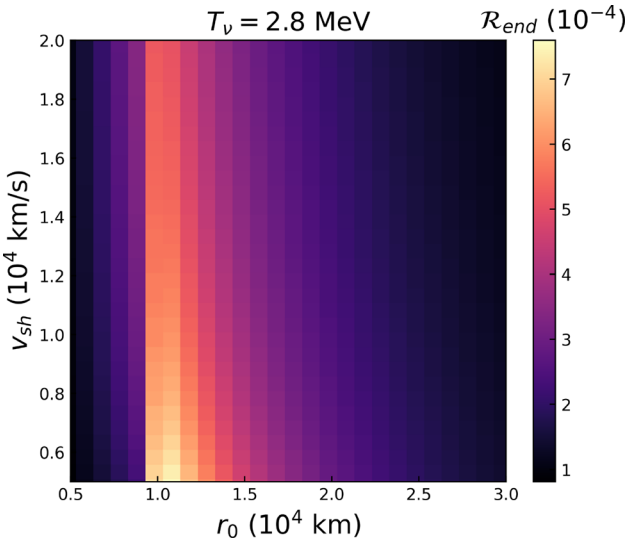

Fig. 26 (Color online) Abundance ratios of ^{26}Al and ^{26}Mg in the process $^{26}\mathrm{Mg}(\nu_e, e^-)^{26}\mathrm{Al}$ for different radii of the O/Ne shell and shock velocities with a neutrino temperature of 2.8 MeV [230]

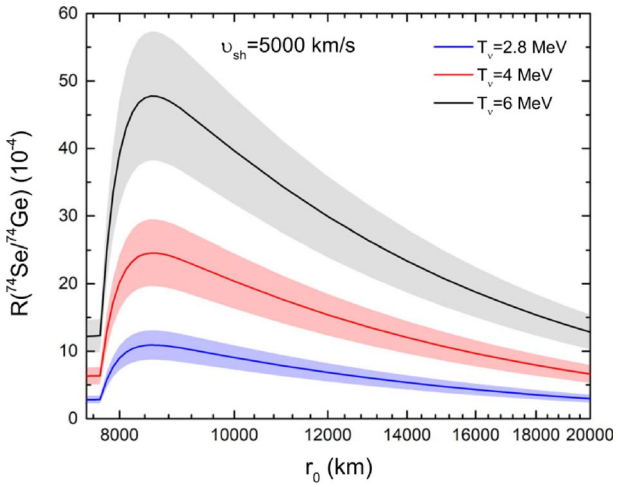

Fig. 27 (Color online) Abundance ratios of ^{74}Se and ^{74}Ge in the process $^{74}\mathrm{Ge}(\nu_e, e^-)^{74}\mathrm{Se}$ varying with the shell radius for different neutrino temperatures [231]

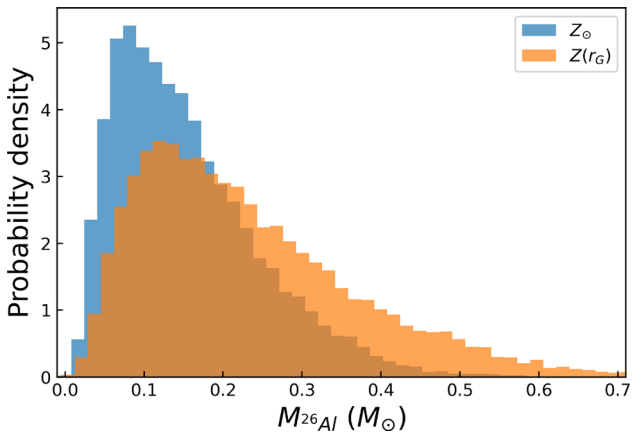

Fig. 28 (Color online) Probability density distributions of the total mass of ^{26}Al produced by the ν_e-process in the Galaxy (including the maximal effects of neutrino flavor oscillations) [230]

7 Summary and outlook

7.1 JUNA Run-2 plan and upgrade

JUNA Run-1 experiments have demonstrated a promising outlook for accurately measuring nuclear astrophysical reactions in underground laboratories. There are still many reactions worth studying in/near the Gamow energy region. In JUNA Run-2, we aim to utilize additional accelerator beam time with higher beam intensities ($\geq$ 1 emA), more radiation-resistant targets, such as diamond targets, and more efficient detection arrays to push the current measurement to lower-energy regions and cover a wider Gamow window. The largest improvement over Run-1 is the use of a windowless gas target, which allows us to choose isotope-enriched gas such as ^{3}He and ^{22}Ne as targets. Once the JUNA experiments resume in 2025, a

plan will be carried out, involving three types of nuclear astrophysics experiments.

The first type will push the holy grail and neutron source reactions to lower energies based on the Run-1 experiments, bringing them closer to the Gamow window.

The second type involves new neutron source reaction and neutrino production reaction measurements, which will use a newly developed windowless gas target that has already been tested on the ground and in accelerator experiments in 2024.

The third type involves other radioactive capture nuclear astrophysics reactions, most of which involve γ-ray measurements.

To perform the above tasks, the JUNA team has upgraded the BGO and ^{3}He detectors, developed new materials such as diamonds for solid radiation-resistant targets, and completed ground accelerator experiment tests.

With the increasing number of experimental proposals and growing activity within the nuclear astrophysics community, it is increasingly challenging to achieve efficient experimental operations relying solely on the JUNA 400-kV accelerator. To fully exploit the benefits of the JUNA deep underground platform, after extensive discussions, the team has proposed a future accelerator plan known as Super-JUNA. The main features of this plan are as follows:

(1) The focus is on maintaining a leading position in at low energy and high current, ensuring the holy grail and neutron source reactions fully span the Gamow window.
(2) To ensure statistical accuracy at low energies and the connection with high-energy ground experiments, the accelerator will be designed with a strength of 20 mA and a maximum voltage of 800 kV.
(3) Considering the selection and technical basis of various accelerations, the accelerator will use an open high-voltage platform consistent with JUNA and reach the above indicators through an optimized ion-source and accelerator tube design.

Super-JUNA is expected to start construction in 2026 and be put into operation in 2028. At that time, Run-3 experiments will be conducted based on JUNA and Run-4 experiments will be concurrently performed based on Super-JUNA. It is expected to achieve comprehensive coverage of important reactions on the "wish list" for direct measurement of deep underground nuclear astrophysics reactions. The establishment of the Super-JUNA platform will provide China with a comprehensive research capability in underground nuclear astrophysics. This platform will address a series of major scientific issues in nuclear astrophysics and become an important center for direct measurements and international collaboration in nuclear astrophysics.

The experimental plan of JUNA Run-2 is shown in Table 5, with the reaction, target, astrophysical environment, and energy range of interest parameters.

7.2 Direct/indirect experiments on ground accelerators

Researchers at the CIAE have conducted extensive indirect/direct experimental research on various ground accelerator facilities. These studies involved various processes in astrophysics, such as H burning, He burning, the *s*-process, *r*-process, and *rp*-process, and have provided important systematic reference data that will highlight the nature of stellar evolution. In the future, with an increase in international cooperation, more extensive research will be conducted on international platforms.

To extend nuclear astrophysics research, BRIF plans to expand further, which will include but not be limited to the following:

(1) Adding a collinear resonance ionization laser spectroscopy and decay measurement device to the ISOL system to measure decay properties for astrophysical r and rp processes.
(2) Expanding the tandem accelerator experimental system to accommodate unstable beam experiments, using a recoil mass spectrometer and superconducting solenoid, etc. to measure astrophysical reactions for *rp*- and *r*-processes.

Looking ahead, the CIAE will continue to realize the BISOL plan. BISOL will use a neutron driver, such as from an accelerator, to achieve fission ions with a ^{235}U target. This acceleration of neutron-rich fission beams will provide opportunities for intense neutron-rich beams, which is crucial for conducting comprehensive studies of reactions and decays along the astrophysical *r*-process. There are many potential locations for BISOL; however, the most attractive is Huizhou, Guangdong. Here, CiADS, which can serve as a driver accelerator, and HIAF, which can serve as part of a post-accelerator, are currently under construction.

7.3 Laser-driven studies on nuclear astrophysics

In recent years, in laser-driven studies on nuclear astrophysics, we have conducted detector calibration for laser nuclear physics experiments. Based on laser facilities such as Shenguang-II, studies on deuterium–deuterium and deuterium–lithium fusion reactions in plasma environments have also been performed. During the research process, a high-efficiency calibration method for neutron detectors

Table 5 Experimental Plan for JUNA Run-2

Experiment	Target type	Astrophysical environment	Studied energies (keV in c.m.)
$^{12}C(\alpha,\gamma)^{16}O$	Solid	Helium burning	450–600
$^{13}C(\alpha,n)^{16}O$	Solid	Neutron source	190–610
$^{19}F(p,\gamma)^{20}Ne$	Solid	CNO cycle	80–150
$^{14}N(p,\gamma)^{15}O$	Solid	CNO cycle	70–280
$^{22}Ne(\alpha,n)^{25}Mg$	Gas	Neutron source	480–710
$^{3}He(\alpha,\gamma)^{7}Be$	Gas	pp-chain	80–380
$^{17}O(p,\alpha)^{14}N$	Solid	CNO cycle	65–75
$^{17}O(p,\gamma)^{18}F$	Solid	CNO cycle	65–360
$^{17}O(\alpha,n)^{20}Ne$	Solid	Neutron source	390–700
$^{26}Al(p,\gamma)^{27}Si$	Solid	Mg-Al cycle	120–350
$^{10}B(\alpha,n)^{13}N$	Solid	Neutron source	220–780

was proposed, and a theoretical model and numerical simulation method suitable for studying nuclear reactions in plasma environments through jet collisions were developed. For the first time, the astrophysical *S*-factor near 173 keV within the Gamow window in a plasma environment was experimentally obtained. The above results promote our understanding of the influence of plasma environments on nuclear reactions and the application of lasers in nuclear physics.

In subsequent research, it is necessary to optimize the quality and stability of beams generated by proton, neutron, and γ-ray lasers and improve the high-repetition rate of these lasers to provide a high-quality source for conducting nuclear reactions. In addition, developing new experimental methods to reduce the impact of strong electromagnetic interference on nuclear reaction parameter measurement is of vital significance. CIAE researchers will continue to develop nuclear radiation detectors suitable for strong electromagnetic environments, measure $^{6}Li(d,n)$ nuclear reactions in plasma environments, and develop related theories and experimental methods.

7.4 Theoretical studies

Studies on supernova nucleosynthesis allow us to decode the evolution of the Universe and the origin of heavy elements from astronomical observations. We investigated the influence of the initial metallicity of the SNe Ia progenitor on the ^{56}Ni yield synthesized during explosions and found that the previous SNe Ia was brighter than the present when they were at the same distance, which would lead to inaccurate distance measurements in cosmology. In addition to this, other factors that may affect nucleosynthesis, such as the rotation of the progenitor and the explosion mechanism of SNe Ia, must also be carefully studied to ensure the accuracy of cosmological measurements, which are the basis for a correct understanding of cosmic evolution history.

In addition, we studied the influences of a powerful neutrino stream on the synthesis of ^{26}Al and ^{74}Se in core-collapse supernovae, which are helpful in exploring the origin of the Galactic ^{26}Al and the formation of the solar system. However, unraveling these mysteries requires more precise theoretical calculations of the synthesis of more nuclides. Furthermore, it requires further clarity on the mechanism of supernova explosions, and correct and precise astrophysical reaction rates are necessary as inputs to the nuclear reaction network [233].

In the future, CIAE researchers will improve the theory and calculation of the nucleosynthesis network and introduce processes such as neutrino physics and fluid dynamics to better explain astrophysical problems, such as the origin of heavy elements. The CIAE will also focus more on expanding the numerical simulation of the impact of reaction rates on the element abundance observation in stars.

Acknowledgements The authors are grateful to the staff of the CJPL and Yalong River Hydropower Development Company, Tsinghua University and Beijing Tandem Accelerator team for laboratory support.

References

1. E.M. Burbidge, G.R. Burbidge, W.A. Fowler et al., Synthesis of the elements in stars. Rev. Mod. Phys. **29**, 547 (1957). https://doi.org/10.1103/RevModPhys.29.547
2. Y.P. Shen, B. Guo, W.P. Liu et al., Alpha-cluster transfer reactions: A tool for understanding stellar helium burning. Prog. Part. Nucl. Phys. **119**, 103857 (2011). https://doi.org/10.1016/j.ppnp.2021.103857
3. R.J. deBoer, J. Görres, M. Wiescher, et al., The $^{12}C(\alpha,\gamma)^{16}O$ reaction and its implications for stellar helium burning. Rev. Mod. Phys. 89 035007 (2017). https://doi.org/10.1103/RevModPhys.89.035007
4. H.M. Xu, C.A. Gagliardi, R.E. Tribble et al., Overall normalization of the astrophysical S factor and the nuclear vertex constant for $^{7}Be(p,\gamma)^{8}B$ reactions. Phys. Rev. Lett. **73**, 2027 (1994). https://doi.org/10.1103/PhysRevLett.73.2027
5. A. Tumino, C.A. Bertulani, M.L. Cognata et al., The Trojan Horse Method: A nuclear physics tool for astrophysics. Annu. Rev. Nucl. Part. Sci. **71**, 345 (2021). https://doi.org/10.1146/annurev-nucl-102419-033642
6. G. Baur, C.A. Bertulani, H. Rebel, Coulomb dissociation as a source of information on radiative capture processes of astrophysical interest. Nucl. Phys. A **458**, 188 (1986). https://doi.org/10.1016/0375-9474(86)90290-3
7. C. Ugalde, B. DiGiovine, D. Henderson et al., First determination of an astrophysical cross section with a bubble chamber: The $^{15}N(\alpha, \gamma)^{19}F$ reaction. Phys. Lett. B **719**, 74 (2013). https://doi.org/10.1016/j.physletb.2012.12.068
8. H. Utsunomiya, S. Goriely, T. Kondo et al., Photoneutron cross sections for Mo isotopes: A step toward a unified understanding of (γ, n) and (n,γ) reactions. Phys. Rev. C **88**, 015805 (2013). https://doi.org/10.1103/PhysRevC.88.015805
9. J. Refsgaard, O.S. Kirsebom, E.A. Dijck et al., Measurement of the branching ratio for β-delayed α decay of ^{16}N. Phys. Lett. B **752**, 296 (2016). https://doi.org/10.1016/j.physletb.2015.11.047
10. P. Tischhauser, A. Couture, R. Detwiler et al., Measurement of elastic $^{12}C + \alpha$ scattering: Details of the experiment, analysis, and discussion of phase shifts. Phys. Rev. C **79**, 055803 (2009). https://doi.org/10.1103/PhysRevC.79.055803
11. C. Broggini, D. Bemmerer, A. Caciolli et al., LUNA: Status and prospects. Prog. Part. Nucl. Phys. **98**, 55 (2018). https://doi.org/10.1016/j.ppnp.2017.09.002
12. M. Aliotta, A. Boeltzig, R. Depalo et al., Exploring stars in underground laboratories: Challenges and solutions. Annu. Rev. Nucl. Part. Sci. **72**, 177 (2022). https://doi.org/10.1146/annurev-nucl-110221-103625
13. M. Junker, G. Imbriani, A. Best et al., The deep underground Bellotti Ion Beam Facility-status and perspectives. Front. Phys. **11**, 1291113 (2023). https://doi.org/10.3389/fphy.2023.1291113
14. D. Robertson, M. Couder, U. Greife et al., Underground nuclear astrophysics studies with CASPAR. EPJ Web Conf. **109**, 09002 (2016). https://doi.org/10.1051/epjconf/201610909002
15. W. Liu, Z. Li, J. He et al., Progress of Jinping Underground laboratory for Nuclear Astrophysics (JUNA). Sci. China-Phys. Mech. Astron. **59**, 642001 (2016). https://doi.org/10.1007/s11433-016-5785-9
16. W. P. Liu, First Results from the Underground Nuclear Reaction Experiments in JUNA. Chin. Phys. Lett. **40**, 060401 (2023). https://doi.org/10.1088/0256-307X/40/6/060401
17. M. Wiescher, W.P. Liu, Deep underground accelerators for studying near-threshold quantum effects in hot stellar plasmas. Sci. Bull. **68**, 666 (2023). https://doi.org/10.1016/j.scib.2023.03.010
18. D. Bemmerer, T.E. Cowan, A. Domula et al., The new Felsenkeller 5 MV underground accelerator. In Solar Neutrinos, ed. by K Zuber, M Meyer (World Scientific, Singapore, 2019), pp. 249–263 (2019). 10.1142/9789811204296_0015
19. J. Skowronski, E. Masha, D. Piatti et al., Improved S factor of the $^{12}C(p,\gamma)^{13}N$ reaction at E = 320–620 keV and the 422 keV resonance. Phys. Rev. C **107**, L062801 (2023). https://doi.org/10.1103/PhysRevC.107.L062801
20. F. Kappeler, R. Gallino, S. Bisterzo et al., The s process: Nuclear physics, stellar models, and observations. Rev. Mod. Phys. **83**, 157 (2011). https://doi.org/10.1103/revmodphys.83.157
21. J.J. Cowan, C. Sneden, J.E. Lawler et al., Origin of the heaviest elements: The rapid neutron-capture process. Rev. Mod. Phys. **93**, 015002 (2021). https://doi.org/10.1103/RevModPhys.93.015002
22. Z.H. Li, W.P. Liu, X.X. Bai et al., The $^{8}Li(d, p)^{9}Li$ reaction and the astrophysical $^{8}Li(n,\gamma)^{9}Li$ reaction rate. Phys. Rev. C **71**, 052801(R) (2005). https://doi.org/10.1103/PhysRevC.71.052801
23. J.E. Escher, J.T. Harke, F.S. Dietrich et al., Compound-nuclear reaction cross sections from surrogate measurements. Rev. Mod. Phys. **84**, 353 (2012). https://doi.org/10.1103/RevModPhys.84.353
24. R. Hatarik, L.A. Bernstein, J.A. Cizewski et al., Benchmarking a surrogate reaction for neutron capture. Phys. Rev. C **81**, 011602(R) (2010). https://doi.org/10.1103/PhysRevC.81.011602
25. A. Spyrou, S.N. Liddick, A.C. Larsen et al., Novel technique for constraining r-process (n,γ) reaction rates. Phys. Rev. Lett. **113**, 232502 (2014). https://doi.org/10.1103/PhysRevLett.113.232502
26. M. Horn, E.L. Woodward, Sanford Underground Research Facility's approach to school education, community activities, and public outreach. Front. Phys. **11**, 1310451 (2023). https://doi.org/10.3389/fphy.2023.1310451
27. J.-P. Cheng, K.-J. Kang, J.-M. Li et al., The China Jinping Underground Laboratory and its early science. Annu. Rev. Nucl. Part. Sci. **67**, 231 (2015). https://doi.org/10.1146/annurev-nucl-102115-044842
28. Y.-J. Chen, H. Zhang, L.-Y. Zhang et al., Direct measurement of the break-out $^{19}F(p,\gamma)^{20}Ne$ reaction in the China Jinping underground laboratory (CJPL). Nucl. Sci. Tech. **35**, 143 (2024). https://doi.org/10.1007/s41365-024-01531-0
29. Z.-L. Shen, J.-J. He, Study of primordial deuterium abundance in Big Bang nucleosynthesis. Nucl. Sci. Tech. **35**, 63 (2024). https://doi.org/10.1007/s41365-024-01423-3
30. Y.J. Chen, L.Y. Zhang, Examining the fluorine overabundance problem by conducting Jinping deep underground experiment. Nucl. Tech. (in Chinese) **46**, 110501 (2023). https://doi.org/10.11889/j.0253-3219.2023.hjs.46.110501
31. Y.F. Wang, J.X. Liu, L.T. Yang et al., Rare physical events at China Jinping underground laboratory. Nucl. Tech. (in Chinese) **46**, 080018 (2023). https://doi.org/10.11889/j.0253-3219.2023.hjs.46.080018
32. T. Kajino, Underground laboratory JUNA shedding light on stellar nucleosynthesis. Nucl. Sci. Tech. **34**, 42 (2023). https://doi.org/10.1007/s41365-023-01196-1
33. J.J. He, S.W. Xu, S.B. Ma et al., A proposed direct measurement of cross section at Gamow window for key reaction $^{19}F(p,\alpha)^{16}O$ in Asymptotic Giant Branch stars with a planned accelerator in CJPL. Sci. China-Phys. Mech. Astron. **59**, 652001 (2016). https://doi.org/10.1007/s11433-016-5797-5
34. Q. Wu, L.T. Sun, B.Q. Cui et al., Design of an intense ion source and LEBT for Jinping Underground Nuclear Astrophysics experiments. Nucl. Instrum. Methods Phys. Res. A **830**, 214 (2016). https://doi.org/10.1016/j.nima.2016.05.099

35. A. Best, J. Görres, M. Junker et al., Low energy neutron background in deep underground laboratories. Nucl. Instrum. Methods Phys. Res. A **812**, 1 (2016). https://doi.org/10.1016/j.nima.2015.12.034
36. A. Sen, G. Domínguez-Cañizares, N.C. Podaru et al., A high intensity, high stability 3.5 MV Singletron^{TM} accelerator. Nucl. Instrum. Methods Phys. Res. B **450**, 390 (2019). https://doi.org/10.1016/j.nimb.2018.09.016
37. D.-M. Mei, A. Hime, Muon-induced background study for underground laboratories. Phys. Rev. D **73**, 053004 (2006). https://doi.org/10.1103/PhysRevD.73.053004
38. M. Aliotta, R. Buompane, M. Couder et al., The status and future of direct nuclear reaction measurements for stellar burning. J. Phys. G Nucl. Part. Phys. **49**, 010501 (2022). https://doi.org/10.1088/1361-6471/ac2b0f
39. J.Q. Li, L.T. Sun, Y. Yang et al., Development of an all permanent magnet ECR ion source for low and medium charge state ions production. J. Phys. Conf. Ser. **1401**, 012022 (2020). https://doi.org/10.1088/1742-6596/1401/1/012022
40. L.H. Wang, J. Su, Y.P. Shen et al., Measurement of the $^{18}O(\alpha,\gamma)^{22}Ne$ reaction rate at JUNA and its impact on probing the origin of SiC grains. Phys. Rev. Lett. **130**, 092701 (2023). https://doi.org/10.1103/PhysRevLett.130.092701
41. Y.P. Shen, J. Su, W.P. Liu et al., Measurement of γ detector backgrounds in the energy range of 3–8 MeV at Jinping underground laboratory for nuclear astrophysics. Sci. China-Phys. Mech. Astron. **60**, 102022 (2017). https://doi.org/10.1007/s11433-017-9049-3
42. Y.-T. Li, W.-P. Lin, B.-S. Gao et al., Development of a low-background neutron detector array. Nucl. Sci. Tech. **33**, 41 (2022). https://doi.org/10.1007/s41365-022-01030-0
43. B. Gao, T.Y. Jiao, Y.T. Li et al., Deep underground laboratory measurement of $^{13}C(\alpha,n)^{16}O$ in the Gamow windows of the s and i processes. Phys. Rev. Lett. **129**, 132701 (2022). https://doi.org/10.1103/physrevlett.129.132701
44. L.H. Wang, Y.P. Shen, J. Su et al., Development of irradiation-resistant enriched ^{12}C targets for astrophysical $^{12}C(\alpha,\gamma)^{16}O$ reaction measurements. Nucl. Instrum. Methods Phys. Res. B. **512**, 49 (2022). https://doi.org/10.1016/j.nimb.2021.11.020
45. C. Chen, Y.-J. Li, H. Zhang et al., Preparation of large-area isotopic magnesium targets for the $^{25}Mg(p,\gamma)^{26}Al$ experiment at JUNA. Nucl. Sci. Tech. **31**, 91 (2020). https://doi.org/10.1007/s41365-020-00800-y
46. L.Y. Zhang, S.W. Xu, J.J. He et al., Properties of fluorine targets and their application on the astrophysically important $^{19}F(p,\alpha)^{16}O$ reaction. Nucl. Instrum. Methods Phys. Res. B. **438**, 48 (2019). https://doi.org/10.1016/j.nimb.2018.10.024
47. L.Y. Zhang, Y.J. Chen, J.J. He et al., Strong and durable fluorine-implanted targets developed for deep underground nuclear astrophysical experiments. Nucl. Instrum. Methods Phys. Res. B. **496**, 9 (2021). https://doi.org/10.1016/j.nimb.2021.03.017
48. L.Y. Zhang, J. Su, J.J. He et al., Direct measurement of the astrophysical $^{19}F(p,\alpha\gamma)^{16}O$ reaction in the deepest operational underground laboratory. Phys. Rev. Lett. **127**, 152702 (2021). https://doi.org/10.1103/PhysRevLett.127.152702
49. L. Zhang, J. He, R.J. deBoer et al., Measurement of $^{19}F(p,\gamma)^{20}Ne$ reaction suggests CNO breakout in first stars. Nature **610**, 656 (2022). https://doi.org/10.1038/s41586-022-05230-x
50. J. Su, H. Zhang, Z.H. Li et al., First result from the Jinping Underground Nuclear Astrophysics experiment JUNA: precise measurement of the 92 keV $^{25}Mg(p,\gamma)^{26}Al$ resonance. Sci. Bull. **67**, 125 (2022). https://doi.org/10.1016/j.scib.2021.10.018
51. T.A. Weaver, S.E. Woosley, Nucleosynthesis in massive stars and the $^{12}C(\alpha,\gamma)^{16}O$ reaction rate. Phys. Rep. **227**, 65 (1993). https://doi.org/10.1016/0370-1573(93)90058-l
52. G. Wallerstein, I. Iben, P. Parker et al., Synthesis of the elements in stars: forty years of progress. Rev. Mod. Phys. **69**, 995 (1997). https://doi.org/10.1103/RevModPhys.69.995
53. R. Farmer, M. Renzo, S.E. de Mink et al., Mind the gap: The location of the lower edge of the pair-instability supernova black hole mass gap. Astrophys. J. **887**, 53 (2019). https://doi.org/10.3847/1538-4357/ab518b
54. R. Farmer, M. Renzo, S.E. de Mink et al., Constraints from gravitational-wave detections of binary black hole mergers on the $^{12}C(\alpha,\gamma)^{16}O$ rate. Astrophys. J. Lett. **902**, L36 (2020). https://doi.org/10.3847/2041-8213/abbadd
55. S.E. Woosley, A. Heger, T.A. Weaver, The evolution and explosion of massive stars. Rev. Mod. Phys. **74**, 1015 (2002). https://doi.org/10.1103/RevModPhys.74.1015
56. M. Fey, Im Brennpunkt der nuklearen Astrophysik: die Reaktion $^{12}C(\alpha,\gamma)^{16}O$, PhD thesis, Stuttgart, Germany (2004)
57. J.W. Hammer, M. Fey, R. Kunz et al., New determination of the $^{12}C(\alpha,\gamma)^{16}O$ reaction rate from γ-ray angular distribution measurements. Nucl. Phys. A. **752**, 514 (2005). https://doi.org/10.1016/j.nuclphysa.2005.02.056
58. J.W. Hammer, M. Fey, R. Kunz et al., E1 and E2 capture cross section and astrophysical reaction rate of the key reaction $^{12}C(\alpha,\gamma)^{16}O$. Nucl. Phys. A. **758**, 363 (2005). https://doi.org/10.1016/j.nuclphysa.2005.05.066
59. R. Plag, R. Reifarth, M. Heil et al., $^{12}C(\alpha,\gamma)^{16}O$ studied with the Karlsruhe 4π BaF_2 detector. Phys. Rev. C **86**, 015805 (2012). https://doi.org/10.1103/PhysRevC.86.015805
60. D.B. Sayre, C.R. Brune, D.E. Carter et al., *E*2 interference effects in the $^{12}C(\alpha,\gamma)^{16}O$ reaction. Phys. Rev. Lett. **109**, 142501 (2012). https://doi.org/10.1103/PhysRevLett.109.142501
61. D. Schürmann, A. Di Leva, L. Gialanella et al., Study of the 6.05 MeV cascade transition in $^{12}C(\alpha,\gamma)^{16}O$. Phys. Lett. B **703**, 557 (2011). https://doi.org/10.1016/j.physletb.2011.08.061
62. D. Schürmann, A. Di Leva, L. Gialanella et al., First direct measurement of the total cross-section of $^{12}C(\alpha,\gamma)^{16}O$. Eur. Phys. J. A **26**, 301 (2005). https://doi.org/10.1140/epja/i2005-10175-2
63. H. Makii, Y. Nagai, T. Shima et al., *E*1 and *E*2 cross sections of the $^{12}C(\alpha,\gamma_0)^{16}O$ reaction using pulsed α beams. Phys. Rev. C **80**, 065802 (2009). https://doi.org/10.1103/PhysRevC.80.065802
64. C. Matei, C. R. Brune, T. N. Massey, Measurements of branching ratios from the 7.12-MeV state in ^{16}O and the $^{12}C(\alpha,\gamma)^{16}O$ reaction cross section, Phys. Rev. C **78**, 065801 (2008).https://doi.org/10.1103/PhysRevC.78.065801
65. M. Assunção, M. Fey, A. Lefebvre-Schuhl et al., *E*1 and *E*2 S factors of $^{12}C(\alpha,\gamma_0)^{16}O$ from γ-ray angular distributions with a 4π-detector array. Phys. Rev. C **73**, 055801 (2006). https://doi.org/10.1103/PhysRevC.73.055801
66. R. Kunz, M. Jaeger, A. Mayer et al., $^{12}C(\alpha,\gamma)^{16}O$: The key reaction in stellar nucleosynthesis. Phys. Rev. Lett. **86**, 3244 (2001). https://doi.org/10.1103/PhysRevLett.86.3244
67. G. Roters, C. Rolfs, F. Strieder et al., The *E*1 and *E*2 capture amplitudes in $^{12}C(\alpha,\gamma_0)^{16}O$. Eur. Phys. J. A **6**, 451 (1999). https://doi.org/10.1007/s100500050369
68. J.M.L. Ouellet, M.N. Butler, H.C. Evans et al., $^{12}C(\alpha,\gamma)^{16}O$ cross sections at stellar energies. Phys. Rev. C **54**, 1982 (1996). https://doi.org/10.1103/PhysRevC.54.1982
69. A. Redder, H.W. Becker, C. Rolfs et al., The $^{12}C(\alpha,\gamma)^{16}O$ cross section at stellar energies. Nucl. Phys. A **462**, 385 (1987). https://doi.org/10.1016/0375-9474(87)90555-0
70. P. Dyer, C.A. Barnes, The $^{12}C(\alpha,\gamma)^{16}O$ reaction and stellar helium burning. Nucl. Phys. A **233**, 495 (1974). https://doi.org/10.1016/0375-9474(74)90470-9

71. B.S. Meyer, The r-, s-, and p-processes in nucleosynthesis. Annu. Rev. Astron. Astr. **32**, 153 (1994). https://doi.org/10.1146/annurev.aa.32.090194.001101
72. C. Sneden, J.J. Cowan, R. Gallino, Neutron-capture elements in the early galaxy. Annu. Rev. Astron. Astr. **46**, 241 (2008). https://doi.org/10.1146/annurev.astro.46.060407.145207
73. J.J. Cowan, W.K. Rose, Production of ^{14}C and neutrons in red giants. Astrophys. J. **212**, 149 (1977). https://doi.org/10.1086/155030
74. M. Hampel, R.J. Stancliffe, M. Lugaro et al., The intermediate neutron-capture process and carbon-enhanced metal-poor stars. Astrophys. J. **831**, 171 (2016). https://doi.org/10.3847/0004-637X/831/2/171
75. S. Cristallo, M. La Cognata, C. Massimi et al., The Importance of the ^{13}C(α,n)^{16}O Reaction in Asymptotic Giant Branch Stars. Astrophys. J. **859**, 105 (2018). https://doi.org/10.3847/1538-4357/aac177
76. A. Choplin, L. Siess, S. Goriely, The intermediate neutron capture process. Astron. Astrophys. **648**, a119 (2021). https://doi.org/10.1051/0004-6361/202040170
77. S. Goriely, L. Siess, A. Choplin, The intermediate neutron capture process. Astron. Astrophys. **654**, a129 (2021). https://doi.org/10.1051/0004-6361/202141575
78. G.F. Ciani, L. Csedreki, D. Rapagnani et al., Direct measurement of the ^{13}C$(\alpha, \mathrm{n})^{16}$O cross section into the *s*-process gamow peak. Phys. Rev. Lett. **127**, 152701 (2021). https://doi.org/10.1103/PhysRevLett.127.152701
79. M. Busso, R. Gallino, G.J. Wasserburg, Nucleosynthesis in asymptotic giant branch stars: Relevance for galactic enrichment and solar system formation. Annu. Rev. Astron. Astr. **37**, 239 (1999). https://doi.org/10.1146/annurev.astro.37.1.239
80. F. Herwig, Evolution of asymptotic giant branch stars. Annu. Rev. Astron. Astr. **43**, 435 (2005). https://doi.org/10.1146/annurev.astro.43.072103.150600
81. R.S. Lewis, S. Amari, E. Anders, Interstellar grains in meteorites: II. SiC and its noble gases. Geochim. Cosmochim. Ac. **58**, 471 (1994). https://doi.org/10.1016/0016-7037(94)90478-2
82. A.C. Dombos, D. Robertson, A. Simon et al., Measurement of low-energy resonance strengths in the ^{18}O(α,γ)^{22}Ne reaction. Phys. Rev. Lett. **128**, 162701 (2022). https://doi.org/10.1103/physrevlett.128.162701
83. S.E. Woosley, W.C. Haxton, Supernova neutrinos, neutral currents and the origin of fluorine. Nature **334**, 45 (1988). https://doi.org/10.1038/334045a0
84. A. Jorissen, V.V. S. Lambert, D.L., Fluorine in red giant stars - Evidence for nucleosynthesis. Astron. Astrophys. **261**, 164–187 (1992).
85. M. Lugaro, C. Ugalde, A.I. Karakas et al., Reaction rate uncertainties and the production of ^{19}F in asymptotic giant branch stars. Astrophys. J. **615**, 934 (2004). https://doi.org/10.1086/424559
86. G. Meynet, M. Arnould, Synthesis of ^{19}F in Wolf-Rayet stars. Astron. Astrophys. **355**, 176 (2000)
87. C. Kobayashi, N. Izutani, A.I. Karakas et al., Evolution of fluorine in the Galaxy with the ν-process. Astrophys. J. Lett. **739**, L57 (2011). https://doi.org/10.1088/2041-8205/739/2/L57
88. L.Y. Zhang, A.Y. López, M. Lugaro et al., Thermonuclear ^{19}F(p,α)^{16}O reaction rate revised and astrophysical implications. Astrophys. J. **913**, 51 (2021). https://doi.org/10.3847/1538-4357/abef63
89. S. Lucatello, T. Masseron, J.A. Johnson et al., Fluorine and sodium in C-rich low-metallicity stars. Astrophys. J. **729**, 40 (2011). https://doi.org/10.1088/0004-637x/729/1/40
90. C. Abia, K. Cunha, S. Cristallo et al., The first fluorine abundance determinations in extragalactic asymptotic giant branch carbon stars. Astrophys. J. Lett. **737**, l8 (2011). https://doi.org/10.1088/2041-8205/737/1/l8
91. J. He, S. Xu, S. Ma et al., A proposed direct measurement of cross section at Gamow window for key reaction ^{19}F(p,α) ^{16}O in Asymptotic Giant Branch stars with a planned accelerator in CJPL. Sci. China-Phys. Mech. Astron. **59**, 652001 (2016). https://doi.org/10.1007/s11433-016-5797-5
92. K. Spyrou, C. Chronidou, S. Harissopulos et al., Cross section and resonance strength measurements of ^{19}F(p,$\alpha\gamma$)^{16}O at E_p= 200–800 keV. Eur. Phys. J. A **7**, 79 (2000). https://doi.org/10.1007/s100500050014
93. L.Y. Zhang, J. Su, J.J. He et al., Direct measurement of the astrophysical ^{19}F$(\mathrm{p}, \alpha\gamma)^{16}$O reaction in a deep-underground laboratory. Phys. Rev. C. **106**, 055803 (2022). https://doi.org/10.1103/PhysRevC.106.055803
94. R.J. deBoer, O. Clarkson, A.J. Couture et al., ^{19}F(p,γ)^{20}Ne and ^{19}F(p,α)^{16}O reaction rates and their effect on calcium production in Population III stars from hot CNO breakout. Phys. Rev. C. **103**, 055815 (2021). https://doi.org/10.1103/PhysRevC.103.055815
95. W.A. Mahoney, J.C. Ling, A.S. Jacobson et al., Diffuse galactic gamma-ray line emission from nucleosynthetic Fe-60, Al-26, and Na-22 - Preliminary limits from HEAO 3. Astrophys. J. **262**, 742 (1982). https://doi.org/10.1086/160469
96. W.A. Mahoney, J.C. Ling, W.A. Wheaton et al., HEAO 3 discovery of Al-26 in the interstellar medium. Astrophys. J. **286**, 578 (1984). https://doi.org/10.1086/162632
97. R. Diehl, D.H. Hartmann, N. Prantzos, eds., Astrophysics with radioactive isotopes. Softcover reprint of the original 2nd ed. 2018 edition, Springer, 2019
98. R. Diehl, C. Dupraz, K. Bennett et al., COMPTEL observations of galactic ^{26}Al emission. Astron. Astrophys. **298**, 445 (1995)
99. R. Diehl, H. Halloin, K. Kretschmer et al., Radioactive ^{26}Al from massive stars in the Galaxy. Nature **439**, 45 (2006). https://doi.org/10.1038/nature04364
100. H. Norgaard, Al-26 from red giants. Astrophys. J. **236**, 895 (1980). https://doi.org/10.1086/157815
101. J.M. Carpenter, M.R. Meyer, C. Dougados et al., Properties of the monoceros R2 stellar cluster. Astrophys. J. **114**, 198 (1997). https://doi.org/10.1086/118465
102. I. Nofar, G. Shaviv, S. Starrfield, The formation of ^{26}Al Nova Explosions. Astrophys. J. **369**, 440 (1991). https://doi.org/10.1086/169772
103. M. Limongi, A. Chieffi, The nucleosynthesis of ^{26}Al and ^{60}Fe in solar metallicity stars extending in mass from 11 to 120 $M_{\odot}$: The hydrostatic and explosive contributions. Astrophys. J. **647**, 483 (2006). https://doi.org/10.1086/505164
104. F. Strieder, B. Limata, A. Formicola et al., The ^{25}Mg(p,γ)^{26}Al reaction at low astrophysical energies. Phys. Lett. B. **707**, 60 (2012). https://doi.org/10.1016/j.physletb.2011.12.029
105. O. Straniero, G. Imbriani, F. Strieder et al., Impact of a revised ^{25}Mg(p,γ)^{26}Al reaction rate on the operation of the Mg-Al cycle. Astrophys. J. **763**, 100 (2013). https://doi.org/10.1088/0004-637x/763/2/100
106. W. Rapp, J. Görres, M. Wiescher et al., Sensitivity of *p*-process nucleosynthesis to nuclear reaction rates in a 25 $M_{\odot}$ supernova model. Astrophys. J. **653**, 474 (2006). https://doi.org/10.1086/508402
107. T. Rauscher, Branchings in the γ process path revisited. Phys. Rev. C **73**, 015804 (2006). https://doi.org/10.1103/PhysRevC.73.015804
108. S.J. Quinn, A. Spyrou, A. Simon et al., Probing the production mechanism of the light *p*-process nuclei. Phys. Rev. C **88**, 011603(R) (2013). https://doi.org/10.1103/PhysRevC.88.011603

109. D. Wu, N.Y. Wang, B. Guo et al., New measurement of the ^{74}Ge(p, γ)^{75}As reaction cross sections in the p-process nucleosynthesis. Phys. Lett. B **805**, 135431 (2020). https://doi.org/10.1016/j.physletb.2020.135431
110. D. Wu, B. Guo, C.Y. He et al., Determination of the ^{74}Ge(p, γ)^{75}As reaction rates in p-process nucleosynthesis with in-beam γ spectroscopy. Nucl. Phys. A **1027**, 122357 (2022). https://doi.org/10.1016/j.nuclphysa.2021.122357
111. A. Anttila, J. Keinonen, M. Hautala et al., Use of the ^{27}Al(p, γ)^{28}Si, E_p = 992 keV resonance as a gamma-ray intensity standard. Nucl. Instrum. Methods **147**, 501 (1977). https://doi.org/10.1016/0029-554X(77)90393-7
112. A. Sauerwein, J. Endres, L. Netterdon et al., Investigation of the reaction ^{74}Ge(p, γ)^{75}As using the in-beam method to improve reaction network predictions for p nuclei. Phys. Rev. C **86**, 035802 (2012). https://doi.org/10.1103/PhysRevC.86.035802
113. J.Y.H. Li, Y. J. Li, Z.H. Li et al., Nuclear astrophysics research based on HI-13 tandem accelerator. Nucl. Tech. (in Chinese) **46**, 080002 (2023). https://doi.org/10.11889/j.0253-3219.2023.hjs.46.080002
114. W.K. Nan, Y. B. Wang, Y. D. Sheng, et al., Novel thick-target kinematics method for the astrophysical ^{12}C+^{12}C fusion reaction. Nucl. Sci. Tech. **35**, 208 (2024). https://doi.org/10.1007/s41365-024-01573-4
115. M. Freer, The clustered nucleus-cluster structures in stable and unstable nuclei. Rep. Prog. Phys. **70**, 2149 (2007). https://doi.org/10.1088/0034-4885/70/12/R03
116. Y.P. Shen, B. Guo, Z.H. Li et al., Astrophysical S_{E2} factor of the ^{12}C(α,γ)^{16}O reaction through the ^{12}C(^{11}B,^{7}Li)^{16}O transfer reaction. Phys. Rev. C. **99**, 025805 (2019). https://doi.org/10.1103/PhysRevC.99.025805
117. Y. P. Shen, B. Guo, R. J. deBoer et al., Constraining the external capture to the ^{16}O ground state and the $E2$ S factor of the ^{12}C(α,γ)^{16}O reaction. Phys. Rev. Lett. 124, 162701 (2020). https://doi.org/10.1103/PhysRevLett.124.162701
118. W. Nan, Y.P. Shen, B. Guo et al., New determination of the astrophysical S_{E1} factor of the ^{12}C(α,γ)^{16}O reaction via the ^{12}C(^{11}B,^{7}Li)^{16}O transfer reaction. Phys. Rev. C **109**, 045808 (2024). https://doi.org/10.1103/PhysRevC.109.045808
119. Z.C. Li, Y.H. Cheng, C. Yan et al., Beijing Q3D magnetic spectrometer and its applications. Nucl. Instrum. Methods Phys. Res. A **336**, 150 (1993). https://doi.org/10.1016/0168-9002(93)91091-Z
120. I.J. Thompson, Coupled reaction channels calculations in nuclear physics. Comput. Phys. Rep. **7**, 167 (1988). https://doi.org/10.1016/0167-7977(88)90005-6
121. D.Y. Pang, Y.L. Ye, F.R. Xu, Application of the Bruyeres Jeukenne-Lejeune-Mahaux model potential to composite nuclei with a single-folding approach. Phys. Rev. C **83**, 064619 (2011). https://doi.org/10.1103/PhysRevC.83.064619
122. Y.P. Xu, D.Y. Pang, Toward a systematic nucleus-nucleus potential for peripheral collisions. Phys. Rev. C **87**, 044605 (2013). https://doi.org/10.1103/PhysRevC.87.044605
123. B.A. Brown, New Skyrme interaction for normal and exotic nuclei. Phys. Rev. C **58**, 220 (1998). https://doi.org/10.1103/PhysRevC.58.220
124. G.R. Satchler, A comparative study of the scattering of light heavy ions using a folding model. Nucl. Phys. A **329**, 233 (1979). https://doi.org/10.1016/0375-9474(79)90292-6
125. E. Bauge, J.P. Delaroche, M. Girod, Lane-consistent, semimicroscopic nucleon-nucleus optical model. Phys. Rev. C **63**, 024607 (2001). https://doi.org/10.1103/PhysRevC.63.024607
126. Y.P. Shen, B. Guo, T.L. Ma et al., First experimental constraint of the spectroscopic amplitudes for the α-cluster in the ^{11}B ground state. Phys. Lett. B **797**, 134820 (2019). https://doi.org/10.1016/j.physletb.2019.134820
127. Y. P. Shen, B. Guo, R. J. deBoer et al., New determination of the ^{12}C(α,γ)^{16}O reaction rate and its impact on the black-hole mass gap. Astrophys. J. **945**, 41 (2023). https://doi.org/10.3847/1538-4357/acb7de
128. R. J. deBoer, J. Görres, M. Wiescher et al., The ^{12}C(α,γ)^{16}O reaction and its implications for stellar helium burning. Rev. Mod. Phys. **89**, 035007 (2017). https://doi.org/10.1103/RevModPhys.89.035007
129. A.K. Mehta, A. Buonanno, J. Gair et al., Observing intermediate-mass black holes and the upper stellar-mass gap with LIGO and Virgo. Astrophys. J. **924**, 39 (2022). https://doi.org/10.3847/1538-4357/ac3130
130. R. Abbott, T.D. Abbott, F. Acernese et al., GWTC-3: Compact binary coalescences observed by LIGO andVirgo during the second part of the third observing run. Phys. Rev. X **13**, 041039 (2023). https://doi.org/10.1103/PhysRevX.13.041039
131. F. kappler, R. Gallino, S. Bisterzo et al., The s process: Nuclear physics, stellar models. Rev. Mod. Phys. **83**, 157 (2011). https://doi.org/10.1103/RevModPhys.83.157
132. M. Lugaro, G. Tagliente, A.I. Karakas et al., The impact of updated Zr neutron-capture cross sections and new asymptotic giant branch models on our understanding of the s process and the origin of stardust. Astrophys. J. **780**, 95 (2014). https://doi.org/10.1088/0004-637X/780/1/95
133. S. Boyer, D. Dassié, J.N. Wilson et al., Determination of the ^{233}Pa(n, γ) capture cross section up to neutron energies of 1 MeV using the transfer reaction ^{232}Th(^{3}He, p)^{234}Pa. Nucl. Phys. A **775**, 175 (2006). https://doi.org/10.1016/j.nuclphysa.2006.06.013
134. G. Kessedjian, B. Jurado, M. Aiche et al., Neutron-induced fission cross sections of short-lived actinides with the surrogate reaction method. Phys. Lett. B **692**, 297 (2010). https://doi.org/10.1016/j.physletb.2010.07.048
135. V.F. Weisskopf, D.H. Ewing, On the yield of nuclear reactions with heavy elements. Phys. Rev. **57**, 472 (1940). https://doi.org/10.1103/PhysRev.57.472
136. S.Q. Yan, Z.H. Li, Y.B. Wang et al., Examination of the surrogate ratio method for the determination of the ^{93}Zr(n, γ)^{94}Zr cross sections with ^{90,92}Zr(^{18}O,^{16}O) ^{92,94}Zr reactions. Phys. Rev. C **94**, 015804 (2016). https://doi.org/10.1103/PhysRevC.94.015804
137. S.R. Lesher, J.T. Harke, L.A. Bernstein et al., Surrogate ratio method in the actinide region using the $(\alpha, \alpha' f)$ reaction. Phys. Rev. C **79**, 044609 (2009). https://doi.org/10.1103/PhysRevC.79.044609
138. B.L. Goldblum, S.R. Stroberg, J.M. Allmond et al., Indirect determination of the ^{230}Th(n, f) and ^{231}Th(n, f) cross sections for thorium-based nuclear energy systems. Phys. Rev. C **80**, 044610 (2009). https://doi.org/10.1103/PhysRevC.80.044610
139. J.J. Ressler, J.T. Harke, J.E. Escher et al., Surrogate measurement of the ^{238}Pu(n, f) cross section. Phys. Rev. C **83**, 054610 (2011). https://doi.org/10.1103/PhysRevC.83.054610
140. J.E. Escher, F.S. Dietrich, Cross sections for neutron capture from surrogate measurements: An examination of Weisskopf-Ewing and ratio approximations. Phys. Rev. C **81**, 024612 (2010). https://doi.org/10.1103/PhysRevC.81.024612
141. S. Chiba, O. Iwamoto, Verification of the surrogate ratio method. Phys. Rev. C **81**, 044604 (2010). https://doi.org/10.1103/PhysRevC.81.044604
142. S.Q. Yan, Z.H. Li, Y.B. Wang et al., The ^{95}Zr(n, γ)^{96}Zr cross section from the surrogate ratio method and its effect on s-process nucleosynthesis. Astrophys. J. **848**, 98 (2017). https://doi.org/10.3847/1538-4357/aa8c74

143. M. Lugaro, A.M. Davis, R. Gallino et al., Isotopic compositions of strontium, zirconium, molybdenum, and barium in single presolar SiC grains and asymptotic giant branch stars. Astrophys. J. **593**, 486 (2003). https://doi.org/10.1086/376442
144. K. Knie, G. Korschinek, T. Faestermann et al., Indication for supernova produced ^{60}Fe activity on earth. Phys. Rev. Lett. **83**, 18 (1999). https://doi.org/10.1103/PhysRevLett.83.18
145. K. Knie, G. Korschinek, T. Faestermann et al., ^{60}Fe Anomaly in a deep-sea manganese crust and implications for a nearby supernova source. Phys. Rev. Lett. **93**, 171103 (2004). https://doi.org/10.1103/PhysRevLett.93.171103
146. A. Wallner, J. Feige, N. Kinoshita et al., Recent near-Earth supernovae probed by global deposition of interstellar radioactive ^{60}Fe. Nature **532**, 69 (2016). https://doi.org/10.1038/nature17196
147. D. Koll, G. Korschinek, T. Faestermann et al., Interstellar ^{60}Fe in antarctica. Phys. Rev. Lett. **123**, 072701 (2019). https://doi.org/10.1103/PhysRevLett.123.072701
148. P. Ludwig, S. Bishop, R. Egli et al., Time-resolved 2-million-year-old supernova activity discovered in Earth's microfossil record. PNAS **113**, 9232 (2016). https://doi.org/10.1073/pnas.16010401131
149. C. Fitoussi, G.M. Raisbeck, K. Knie et al., Search for supernova-produced ^{60}Fe in a marine sediment. Phys. Rev. Lett. **101**, 12101 (2008). https://doi.org/10.1103/PhysRevLett.101.121101
150. L. Fimiani, D.L. Cook, T. Faestermann et al., Interstellar ^{60}Fe on the surface of the moon. Phys. Rev. Lett. **116**, 151104 (2016). https://doi.org/10.1103/PhysRevLett.116.151104
151. S.Q. Yan, X.Y. Li, K. Nishio et al., The ^{59}Fe$(n,\gamma)^{60}$Fe cross section from the surrogate ratio method and its effect on the ^{60}Fe nucleosynthesis. Astrophys. J. **919**, 84 (2021). https://doi.org/10.3847/1538-4357/ac12ce
152. R. Betts, H. Fortune, D. Pullen, A study of ^{26}Al by the ^{25}Mg(^{3}He,d) reaction. Nucl. Phys. A **299**, 412 (1978). https://doi.org/10.1016/0375-9474(78)90380-9
153. A.E. Champagne, A.J. Howard, M.S. Smith et al., The effect of weak resonances on the ^{25}Mg$(p,\gamma)^{26}$Al reaction rate. Nucl. Phys. A **505**, 384 (1989). https://doi.org/10.1016/0375-9474(89)90382-5
154. A. Rollefson, V. Wijekumar, C. Browne et al., Spectroscopic factors for proton unbound levels in ^{26}Al and their influence on stellar reaction rates. Nucl. Phys. A **507**, 413 (1990). https://doi.org/10.1016/0375-9474(90)90301-2
155. Y. J. Li, Z. H. Li, E. T. Li et al., Indirect measurement of the 57.7 keV resonance strength for the astrophysical γ-ray source of the ^{25}Mg$(p,\gamma)^{26}$Al reaction. Phys. Rev. C **102**, 025804 (2020). https://doi.org/10.1103/physrevc.102.025804
156. L. Gan, Z.H. Li, H.B. Sun et al., Parametrization of woods-saxon potential for heavy-ion systems. Sci. China-Phys. Mech. Astron. **60**, 082013 (2017). https://doi.org/10.1007/s11433-017-9061-5
157. A. Cumming, L. Bildsten, Carbon flashes in the heavy-element ocean on accreting neutron stars. Astrophys. J. **559**, L127 (2001). https://doi.org/10.1086/323937
158. X.D. Tang, L.H. Ru, The ^{12}C+^{12}C fusion reaction at stellar energies. EPJ Web Conf. **260**, 10 (2022). https://doi.org/10.1051/epjconf/202226001002
159. K. Mori, M. A. Famiano, T. Kajino, Impacts of the new carbon fusion cross-sections on type Ia supernovae. MNRAS: Lett. **482**, L70 (2019). https://doi.org/10.1093/mnrasl/sly188
160. B.B. Back, H. Esbensen, C.L. Jiang et al., Recent developments in heavy ion fusion reactions. Rev. Mod. Phys. **86**, 317 (2014). https://doi.org/10.1103/RevModPhys.86.317
161. T.E. Strohmayer, E.F. Brown, A remarkable 3 hour thermonuclear burst from 4u 1820–30. Astrophys. J. **566**, 1045 (2002). https://doi.org/10.1086/338337
162. M. Pignatari, R. Hirschi, M. Wiescher et al., The ^{12}C+^{12}C reaction and the impact on nucleosynthesis in massive stars. Astrophys. J. **762**, 1 (2013). https://doi.org/10.1088/0004-637X/762/1/31
163. R.L. Cooper, A.W. Steiner, E.F. Brown, Possible resonances in the ^{12}C+^{12}C fusion rate and superburst ignition. Astrophys. J. **702**, 660 (2009). https://doi.org/10.1088/0004-637X/702/1/660
164. J.R. Patterson, H. Winkler, C.S. Zaidins et al., Experimental investigation of the stellar nuclear reaction ^{12}C+^{12}C at low energies. Astrophys. J. **157**, 367 (1969). https://doi.org/10.1086/150073
165. H.W. Becker, K.U. Kettner, C. Rolfs et al., The ^{12}C+^{12}C reaction at sub-coulomb energies (II). Z. Phys. A **303**, 305 (1981). https://doi.org/10.1007/BF01421528
166. J. Zickefoose, A.D. Leva, F. Strieder et al., Measurement of the ^{12}C$(^{12}$C, p$)^{23}$Na cross section near the Gamow energy. Phys. Rev. C **97**, 065806 (2018). https://doi.org/10.1103/PhysRevC.97.065806
167. E.F. Aguilera, P. Rosales, E. Martinez-Quiroz et al., New γ-ray measurements for ^{12}C+^{12}C sub-coulomb fusion: Toward data unification. Phys. Rev. C **73**, 064601 (2006). https://doi.org/10.1103/PhysRevC.73.064601
168. T. Spillane, F. Raiola, C. Rolfs et al., ^{12}C+^{12}C fusion reactions near the Gamow energy. Phys. Rev. Lett. **98**, 122501 (2007). https://doi.org/10.1103/PhysRevLett.98.122501
169. L. Barrón-Palos, E.F. Aguilera, J. Aspiazu et al., Absolute cross sections measurement for the ^{12}C+^{12}C system at astrophysically relevant energies. Nucl. Phys. A **779**, 318 (2006). https://doi.org/10.1016/j.nuclphysa.2006.09.004
170. M.D. High, B. Cujec, The ^{12}C+^{12}C sub-coulomb fusion cross section. Nucl. Phys. A **282**, 181 (1977). https://doi.org/10.1016/0375-9474(77)90179-8
171. B. Bucher, X.D. Tang, X. Fang et al., First direct measurement of ^{12}C$(^{12}$C, n$)^{23}$Mg at stellar energies. Phys. Rev. Lett. **114**, 251102 (2015). https://doi.org/10.1103/PhysRevLett.114.251102
172. C.L. Jiang, D. Santiago-Gonzalez, S. Almaraz-Calderon et al., Reaction rate for carbon burning in massive stars. Phys. Rev. C **97**, 012801 (2018). https://doi.org/10.1103/PhysRevC.97.012801
173. G.R. Caughlan, W.A. Fowler, Thermonuclear reaction rates V. Atom. Data Nucl. Data. **40**, 1 (1988). https://doi.org/10.1016/0092-640X(88)90009-5
174. A. Tumino, C. Spitaleri, M.L. Cognata et al., An increase in the ^{12}C + ^{12}C fusion rate from resonances at astrophysical energies. Nature **557**, 687 (2018). https://doi.org/10.1038/s41586-018-0149-4
175. W. K. Nan, Y. B. Wang, Y. P. Shen, et al., The current status of astrophysical S*-factor studies for the ^{12}C+^{12}C fusion reaction. Nucl. Phys. Rev. accepted (2024) (in Chinese) https://chinaxiv.org/abs/202409.00035
176. Y. Taniguchi, M. Kimura, ^{12}C + ^{12}C fusion S*-factor from a full-microscopic nuclear model. Phys. Lett. B **823**, 136790 (2021). https://doi.org/10.1016/j.physletb.2021.136790
177. C.B. Fu, G.Q. Zhang, Y.G. Ma, New opportunities for nuclear and atomic physics on the femto- to nanometer scale with ultra-high-intensity lasers. Matter Radiat. Extrem. **7**(2), 1211–1213 (2015). https://doi.org/10.1063/5.0059405
178. C.B. Fu, J. Bao, L.M. Chen et al., Laser-driven plasma collider for nuclear studies. Sci. Bull. **60**, 024201 (2022). https://doi.org/10.1007/s11434-015-0821-0

179. D.T. Casey, D.B. Sayre, C.R. Brune et al., Thermonuclear reactions probed at stellar-core conditions with laser-based inertial-confinement fusion. Nat. Phys. **13**, 1227–1231 (2017). https://doi.org/10.1038/nphys4220
180. M. Barbui, W. Bang, A. Bonasera et al., Measurement of the plasma astrophysical S factor for the $^{3}\mathrm{He}(\mathrm{d},\mathrm{p})^{4}\mathrm{He}$ reaction in exploding molecular clusters. Phys. Rev. Lett. **111**, 082502 (2013). https://doi.org/10.1103/PhysRevLett.111.082502
181. N. Prantzos, R. Diehl, Radioactive ^{2}6Al in the galaxy: observations versus theory. Phys. Rep. **267**, 1–69 (1996). https://doi.org/10.1016/0370-1573(95)00055-0
182. V.Y. Glebov, T.C. Sangster, C. Stoeckl et al., The national ignition facility neutron time-of-fligh system and its initial performance (invited). Rev. Sci. Instrum. **81**, 10D325 (2010). https://doi.org/10.1063/1.3492351
183. Y.V. Glebov, C. Forrest, J. Knauer et al., Testing a new NIF neutron time-of-flight detector with a bibenzyl scintillator on OMEGA A. Rev. Sci. Instrum. **83**, 10D309 (2012). https://doi.org/10.1063/1.4731001
184. K. Rezac, D. Klir, P. Kubes et al., Improvement of time-of-flight methods for reconstruction of neutron energy spectra from $D(d,n)^{3}$He fusion reactions. Plasma Phys. Control. Fusion **54**, 105011 (2012). https://doi.org/10.1088/0741-3335/54/10/105011
185. X.F. Xi, G.Q. Zhang, F.L. Liu et al., Direct calibration of neutron detectors for laser-driven nuclear reaction experiments with a gated neutron source. Rev. Sci. Instrum. **94**, 013301 (2023)
186. W. Mannhart, Evaluation of the Cf-252 fission neutron spectrum between 0 MeV and 20 MeV. in Proceedings of an Advisory Group Meeting on Properties of Neutron Sources, Leningrad, USSR, 1986, TECDOC-410, edited by K. Okamoto (International Atomic Energy Agency, (1987), p158
187. N.V. Kornilov, I. Fabry, S. Oberstedt et al., Total characterization of neutron detectors with a ^{252}Cf source and a new light output determination. Nucl. Instrum. Methods Phys. Res. A **599**, 226 (2009). https://doi.org/10.1016/j.nima.2008.10.032
188. T. Nishitani, K. Ogawa, M. Isobe et al., Calibration experiment and the neutronics analyses on the LHD neutron flu monitors for the deuterium plasma experiment. Fusion Eng. Des. **136**, 210 (2018). https://doi.org/10.1016/j.fusengdes.2018.01.053
189. K. Skarsvåg, Differential angular distribution of prompt gamma rays from spontaneous fission of ^{252}Cf. Phys. Rev. C **22**, 638 (1980). https://doi.org/10.1103/PhysRevC.22.638
190. M.L. Roush, M.A. Wilson, W.F. Hornyak, Pulse shape discrimination. Nucl. Instrum. Methods **31**, 112 (1964). https://doi.org/10.1016/0029-554X(64)90333-7
191. D. Cester, M. Lunardon, G. Nebbia et al., Pulse shape discrimination with fast digitizers. Nucl. Instrum. Methods Phys. Res. A **748**, 33 (2014). https://doi.org/10.1016/j.nima.2014.02.032
192. H. Chen and F. Zhao, Establishment of microsecond pulse beam system on Cockcroft-Walton accelerator. At. Energy Sci. Technol. 48, 1300 (2014). https://doi.org/10.7538/yzk.2014.48.07.1300 (in Chinese)
193. G. Dietze, H. Klein, Gamma-calibration of NE 213 scintillation counters. Nucl. Instrum. Methods Phys. Res. **193**, 549 (1982). https://doi.org/10.1016/0029-554X(82)90249-X
194. S.-Y.-L.-T. Zhang, Z.Q. Chen, R. Han et al., Study on gamma response function of EJ301 organic liquid scintillator with GEANT4 and FLUKA. Chin. Phys. C **37**, 126003 (2013). https://doi.org/10.1088/1674-1137/37/12/126003
195. L. Chang, Y. Liu, L. Du et al., Pulse shape discrimination and energy calibration of EJ301 liquid scintillation detector. Nucl. Tech. (in Chinese) **38**, 020501 (2015). https://doi.org/10.11889/j.0253-3219.2015.hjs.38.020501
196. A. Muoio, C. Altana, M. Frassetto et al., Nanostructured targets irradiation by ns-laser for nuclear astrophysics applications: first results. J. Inst. **12**, C03076 (2017). https://doi.org/10.1088/1748-0221/12/03/C03076
197. D. Mascali, S. Tudisco, A. Bonanno et al., Colliding laser-produced plasmas: a new tool for nuclear astrophysics studies. Radiat. Eff. Defect. S. **165**, 730 (2010). https://doi.org/10.1080/10420151003729847
198. C.B. Fu, J. Bao, L.M. Chen et al., Laser-driven plasma collider for nuclear studies. Sci. Bull. **60**, 1211 (2015). https://doi.org/10.1007/s11434-015-0821-0
199. X.F. Xi, C. Lv, W.J. Ma et al., Deuterium-deuterium fusion in nanowire plasma driven with a nanosecond high-energy laser. Front. Phys. **11**, 1212293 (2023). https://doi.org/10.3389/fphy.2023.1212293
200. J.R. Zhao, X.P. Zhang, D.W. Yuan et al., Neutron yield enhancement in laser-induced deuterium-deuterium fusion using a novel shaped target. Rev. Sci. Instrum. **86**, 063505 (2015). https://doi.org/10.1063/1.4922912
201. J.R. Zhao, X.P. Zhang, D.W. Yuan et al., A novel laser-collider used to produce monoenergetic 13.3 MeV $^{7}\mathrm{Li}(d,n)$ neutrons. Sci. Rep. **6**, 27363 (2016). https://doi.org/10.1038/srep27363
202. X.P. Zhang, J.R. Zhao, D.W. Yuan et al., Deuteron-deuteron fusion in laser-driven counter-streaming collisionless plasmas. Phys. Rev. C **96**, 055801 (2017). https://doi.org/10.1103/PhysRevC.96.055801
203. Y. Yasutomo, K. Miyata, S.-I. Himeno et al., A new numerical method for asymmetrical abel inversion. IEEE Trans. Plasma Sci. **9**, 18 (1981). https://doi.org/10.1109/TPS.1981.4317374
204. W.Z. Wang, C. Lv, X.P. Zhang et al., First measurement of the $^{7}\mathrm{Li}(d,n)$ astrophysical S-factor in laser-induced full plasma. Phys. Lett. B **843**, 138034 (2023). https://doi.org/10.1016/j.physletb.2023.138034
205. A.G. Riess, A.V. Filippenko, P. Challis et al., Observational evidence from supernovae for an accelerating universe and a cosmological constant. Astron. J. **116**, 1009 (1998). https://doi.org/10.1086/300499
206. B.P. Schmidt, N.B. Suntzeff, M.M. Phillips et al., The high Z supernova search: Measuring cosmic deceleration and global curvature of the universe using type Ia supernovae. Astrophys. J. **507**, 46 (1998). https://doi.org/10.1086/306308
207. S. Perlmutter, G. Aldering, G. Goldhaber et al., Measurements of Ω and Λ from 42 high-redshift supernovae. Astrophys. J. **517**, 565 (1999). https://doi.org/10.1086/307221
208. W.D. Arnett, Type I supernovae. I - Analytic solutions for the early part of the light curve. Astrophys. J. **253**, 785 (1982). https://doi.org/10.1086/159681
209. F.X. Timmes, E.F. Brown, J.W. Truran, On variations in the peak luminosity of type ia supernovae. Astrophys. J. Lett. **590**, L83 (2003). https://doi.org/10.1086/376721
210. E. Bravo, I. Dominguez, C. Badenes et al., Metallicity as a source of dispersion in the SNIa bolometric light curve luminosity-width relationship. Astrophys. J. Lett. **711**, L66 (2010). https://doi.org/10.1088/2041-8205/711/2/L66
211. W. Hillebrandt, J.C. Niemeyer, Type Ia supernova explosion models. Annu. Rev. Astron. Astrophys. **38**, 191 (2000). https://doi.org/10.1146/annurev.astro.38.1.191
212. W. Hillebrandt, M. Kromer, F. K. Röpke et al., Towards an understanding of Type Ia supernovae from a synthesis of theory and observations. Front. Phys. (Beijing) **8**, 116 (2013). https://doi.org/10.1007/s11467-013-0303-2
213. D. Maoz, F. Mannucci, G. Nelemans, Observational clues to the progenitors of Type-Ia supernovae. Ann. Rev. Astron. Astrophys. **52**, 107 (2014). https://doi.org/10.1146/annurev-astro-082812-141031

214. A.J. Ruiter, Type Ia supernova sub-classes and progenitor origin. IAU Symp. **357**, 1 (2019). https://doi.org/10.1017/S1743921320000587
215. G.X. Li, Z.H. Li, Effect of cosmic mean metallicity on the supernovae cosmology. Astron. J. **162**, 249 (2021). https://doi.org/10.3847/1538-3881/ac2cbb
216. C. Badenes, E. Bravo, J.P. Hughes, The end of amnesia: A new method for measuring the metallicity of Type la supernova progenitors using manganese lines in supernova remnants. Astrophys. J. Lett. **680**, L33 (2008). https://doi.org/10.1086/589832
217. C. Badenes, E. Bravo, J.P. Hughes, The end of amnesia: Measuring the metallicities of Type la SN progenitors with manganese lines in supernova remnants. AIP Conf. Proc. **1111**, 307 (2009). https://doi.org/10.1063/1.3141565
218. C. Badenes, J. Harris, D. Zaritsky et al., The stellar ancestry of supernova progenitors in the magellanic clouds - I. the most recent supernovae in the large magellanic cloud. Astrophys. J. **700**, 727 (2009). https://doi.org/10.1088/0004-637X/700/1/727
219. E. Bravo, C. Badenes, Is the metallicity of their host galaxies a good measure of the metallicity of Type Ia supernovae. Mon. Not. Roy. Astron. Soc. **414**, 1592 (2011). https://doi.org/10.1111/j.1365-2966.2011.18498.x
220. R.J. Foley, R.P. Kirshner, Metallicity differences in type Ia supernova progenitors inferred from ultraviolet spectra. Astrophys. J. Lett. **769**, L1 (2013). https://doi.org/10.1088/2041-8205/769/1/L1
221. J.X. Prochaska, E. Gawiser, A.M. Wolfe et al., The Age-metallicity relation of the universe in neutral gas: The First 100 damped Ly-alpha systems. Astrophys. J. Lett. **595**, L9 (2003). https://doi.org/10.1086/378945
222. M. Rafelski, A.M. Wolfe, J.X. Prochaska et al., Metallicity evolution of damped Lyman-alpha systems out to $z \sim 5$. Astrophys. J. **755**, 89 (2012). https://doi.org/10.1088/0004-637X/755/2/89
223. L. Vincoletto, F. Matteucci, F. Calura et al., Cosmic star formation rate: a theoretical approach. Mon. Not. Roy. Astron. Soc. **421**, 3116 (2012). https://doi.org/10.1111/j.1365-2966.2012.20535.x
224. L. Gioannini, F. Matteucci, F. Calura, The cosmic dust rate across the Universe. Mon. Not. Roy. Astron. Soc. **471**, 4615 (2017). https://doi.org/10.1093/mnras/stx1914
225. L. Perivolaropoulos, F. Skara, Challenges for ΛCDM: An update. New Astron. Rev. **95**, 101659 (2022). https://doi.org/10.1016/j.newar.2022.101659
226. S.E. Woosley, D.H. Hartmann, R.D. Hoffman et al., The neutrino process. Astrophys. J. **356**, 272 (1990). https://doi.org/10.1086/168839
227. A.R. Samana, C.A. Barbero, S.B. Duarte et al., Gross theory model for neutrino-nucleus cross section. New J. Phys. **10**, 033007 (2008). https://doi.org/10.1088/1367-2630/10/3/033007
228. I.N. Borzov, S. Goriely, Weak interaction rates of neutron rich nuclei and the r-process nucleosynthesis. Phys. Rev. C **62**, 035501 (2000). https://doi.org/10.1103/PhysRevC.62.035501
229. A. Sieverding, G. Martínez-Pinedo, L. Huther et al., The ν process in the light of an improved understanding of supernova neutrino spectra. Astrophys. J. **865**, 143 (2018). https://doi.org/10.3847/1538-4357/aadd48
230. G.X. Li, Z.H. Li, The ^{26}Al production of the ν_e-process in the explosion of massive stars. Astrophys. J. **932**, 49 (2022). https://doi.org/10.3847/1538-4357/ac6ef8
231. N. Song, S. Zhang, Z.H. Li et al., Influence of neutrino–nuclear reactions on the abundance of ^{74}Se. Astrophys. J. **941**, 56 (2022). https://doi.org/10.3847/1538-4357/aca328
232. R. Diehl, M. Lugaro, A. Heger et al., The radioactive nuclei ^{26}Al and ^{60}Fe in the Cosmos and in the solar system. Public. Astron. Soc. Aust. **38**, e062 (2021). https://doi.org/10.1017/pasa.2021.48
233. H.L. Liu, D.D. Han, Y.G. Ma et al., Network structure of thermonuclear reactions in nuclear landscape. Sci. China-Phys. Mech. Astron. **63**, 112062 (2020). https://doi.org/10.1007/s11433-020-1552-2